

Connecting the Dots: UV-Bright Companions of Little Red Dots as Lyman-Werner Sources Enabling Direct Collapse Black Hole Formation

JOSEPHINE F.W. BAGGEN ,¹ MATTHEW T. SCOGGINS ,² PIETER VAN DOKKUM ,¹ ZOLTÁN HAIMAN ,³
 ALBERTO TORRALBA ,³ AND JORRYT MATTHEE ,³

¹Department of Astronomy, Yale University, New Haven, CT 06511, USA

²Department of Astronomy, Columbia University, 550 West 120th Street, New York, NY, 10027, U.S.A

³Institute of Science and Technology Austria (ISTA), Am Campus 1, 3400 Klosterneuburg, Austria

ABSTRACT

We compile a sample of 83 Little Red Dots (LRDs) with JWST imaging and find that a substantial fraction ($\sim 43\%$, rising to $\gtrsim 85\%$ for the most luminous LRDs) host one or more spatially offset, UV-bright companions at projected separations of $0.5 \text{ kpc} \lesssim d \lesssim 5 \text{ kpc}$, with median $\langle d \rangle = 1.0 \text{ kpc}$. This fraction is even higher when smaller spatial scales are probed at high S/N ratio: we show that the two most strongly lensed LRDs known to date, A383-LRD and the newly discovered A68-LRD, both have UV-bright companions at separations of only $d \sim 0.3 \text{ kpc}$, below the resolution limit of most unlensed JWST samples. We explore whether these ubiquitous red / blue configurations may be physically linked to the formation of LRDs, in analogy with the “synchronized pair” scenario originally proposed for direct-collapse black hole formation. In this picture, ultraviolet radiation from the companions, which typically have modest stellar masses ($M_* \sim 10^{8-9} M_\odot$), suppresses molecular hydrogen cooling in nearby gas, allowing nearly isothermal collapse and the formation of extremely compact objects, such as massive black holes or quasi-stars. Using component-resolved photometry and SED modeling, we infer Lyman-Werner radiation fields of $J_{21,\text{LW}} \sim 10^{2.5-10^5}$ at the locations of the red components, comparable to those required in direct-collapse models, suggesting that the necessary photodissociation conditions are realized in many LRD systems. This framework provides a simple and self-consistent explanation for the extreme compactness and distinctive spectral properties of LRDs, and links long-standing theoretical models for early compact object formation directly to a population now observed with JWST in the early universe.

Keywords: cosmology: observations — galaxies: formation — galaxies: high-redshift — black hole physics

1. INTRODUCTION

The James Webb Space Telescope (JWST) has revealed a population of extremely compact red sources, referred to as Little Red Dots (LRDs; J. Matthee et al. 2024), predominantly found at high redshifts ($z \sim 4-8$). Their unique spectral and morphological properties challenge simple interpretations in which the observed emission arises from normal stellar populations or classical active galactic nuclei (see K. Inayoshi & L. C. Ho 2025; J. Matthee 2025, for detailed discussions).

While dubbed “dots” due to their compact appearance at rest-frame optical wavelengths, LRDs are increasingly revealed to be more complex than single, unresolved

point sources, particularly in filters tracing the rest-frame ultraviolet (UV) (e.g., P. Rinaldi et al. 2024; C.-H. Chen et al. 2025; A. Torralba et al. 2026; F. D’Eugenio et al. 2026; I. Labbe et al. 2024; R. M. Mérida et al. 2025; J. F. W. Baggen et al. 2024, 2025; M. Golubchik et al. 2025). One of the clearest examples of such resolved substructure is observed in A383-LRD, a strongly lensed system behind the galaxy cluster Abell 383 (J. F. W. Baggen et al. 2025; M. Golubchik et al. 2025; K. K. Knudsen et al. 2025). In this case, strong gravitational lensing enables the separation of two compact components that are $\sim 300-400$ pc apart in the source plane, with one component dominating the rest-frame UV with a flat continuum and the other the rest-frame optical, with a very steep “BH*/Cliff”-like SED (R. P. Naidu et al. 2025; A. de Graaff et al. 2025a). The characteristic

V-shaped SED associated with LRDs (e.g. [D. J. Setton et al. 2024](#); [R. E. Hviding et al. 2025](#)) arises from the superposition of these two components. Without the aid of strong gravitational lensing, these components would be blended at typical JWST resolution, making it difficult to disentangle their distinct contributions to the observed SED ([J. F. W. Baggen et al. 2025](#)).

Beyond elucidating the origin of the V-shaped SEDs of LRDs, this configuration raises a more fundamental question: why is an extremely compact red source found in such close proximity to a UV-bright companion? Is this a coincidence, or does it reflect a physical connection that is important for the formation of these enigmatic objects?

Interestingly, theoretical models have long predicted that the formation of extremely compact massive objects in the early Universe requires precisely such environments. In nearly metal-free gas, molecular hydrogen provides the dominant cooling channel, but far-ultraviolet photons in the Lyman-Werner (LW) band can dissociate H₂ via the Solomon process ([B. T. Draine & F. Bertoldi 1996](#)). If the local LW radiation field is sufficiently intense, molecular hydrogen is dissociated, and cooling is suppressed, allowing gas clouds to bypass normal star formation and collapse rapidly at the atomic-cooling threshold ([K. Omukai 2001](#)), avoiding fragmentation ([S. P. Oh & Z. Haiman 2002](#)) and ultimately leading to a massive black hole ([V. Bromm & A. Loeb 2003](#); [M. Volonteri & M. J. Rees 2005](#)). This has been envisioned to occur through the intermediate formation of a supermassive star ([B. Agarwal et al. 2012](#); [M. A. Latif et al. 2013](#); [A. Ferrara et al. 2014](#); [K. Sugimura et al. 2014](#); [T. Hosokawa et al. 2016](#); [S. Chon et al. 2016](#); [S. Hirano et al. 2017](#); [L. Haemmerlé et al. 2018](#)), a short-lived quasi-star phase (e.g. [M. C. Begelman et al. 2006](#); [M. Volonteri & M. C. Begelman 2010](#)), or an extremely dense star cluster (e.g. [K. Omukai et al. 2008](#); [B. Devecchi & M. Volonteri 2009](#); [T. C. N. Boekholt et al. 2018](#); [P. Natarajan 2011](#)). These pathways can all ultimately seed a massive 'heavy seed' black hole (see [M. Volonteri 2010](#); [Z. Haiman 2013](#); [K. Inayoshi et al. 2020](#), for comprehensive reviews), but they rely on the suppression of efficient H₂ cooling and fragmentation of a pristine cloud.

The strength of the LW radiation field is conventionally quantified by the specific intensity J_{21} , expressed in units of $10^{-21} \text{ erg s}^{-1} \text{ cm}^{-2} \text{ Hz}^{-1} \text{ sr}^{-1}$. Molecular cooling is suppressed only when the local LW intensity exceeds a critical threshold, J_{crit} , whose value depends on the spectral shape of the radiation field and the thermochemical state of the gas. Estimates of J_{crit} have spanned a wide range, (e.g. [Z. Haiman et al. 1997](#); [M. E.](#)

[Machacek et al. 2001](#); [K. Omukai 2001](#); [S. P. Oh & Z. Haiman 2002](#); [C. Shang et al. 2010](#); [J. Wolcott-Green et al. 2011](#); [M. A. Latif et al. 2014](#); [K. Inayoshi et al. 2020](#); [B. Agarwal et al. 2016](#)). However, in gas clouds in protogalactic halos with virial temperatures above $\sim 10^4 \text{ K}$, where atomic cooling is activated, allowing the gas to contract to high densities, studies have converged on $J_{\text{crit}} \approx 10^3 J_{21}$ for realistic spectral energy distributions ([K. Sugimura et al. 2014](#); [J. Wolcott-Green et al. 2017](#)). Such intensities far exceed the global UV background, yet they can be achieved in the immediate vicinity of star-forming galaxies, known as the "close synchronized pair" scenario ([M. Dijkstra et al. 2008](#); [E. Visbal et al. 2014](#); [B. Agarwal et al. 2014](#); [J. A. Regan et al. 2017](#)).

Although originally developed to explain the origin of the seeds of supermassive black holes in quasars at $z \sim 6$, the synchronized pair scenario may be relevant for LRDs as well. Recent studies have interpreted LRDs as the outcome of rapid collapse without fragmentation, described variously as direct-collapse black holes, self-gravitating discs accreting onto supermassive stars, or quasi-stars ([F. Pacucci et al. 2026](#); [E. Cenci & M. Habouzit 2025](#); [J. Jeon et al. 2025](#); [Q. Fei et al. 2025](#); [L. Zwick et al. 2025](#); [A. D. Santarelli et al. 2025b](#); [M. C. Begelman & J. Dexter 2025](#)). The steep red rest-frame optical spectra observed in LRDs may reflect the dense gas environments expected after such a collapse ([K. Inayoshi & R. Maiolino 2025](#); [R. P. Naidu et al. 2025](#); [A. de Graaff et al. 2025a](#); [V. Rusakov et al. 2025](#); [X. Ji et al. 2025](#); [A. Sneppen et al. 2026](#)).

If LRDs are indeed the products of this direct collapse process, and have not yet evolved far away from their formation conditions, then they should generally appear in close proximity to UV-bright companions capable of generating J_{21} flux levels exceeding the critical threshold. In this Letter, we test this hypothesis across a large spectroscopic sample of LRDs, including both unlensed deep fields and strongly lensed cluster fields. We search for nearby UV-bright companions around LRDs and quantify whether their ultraviolet output is sufficient to generate intense local LW radiation fields comparable to those required by theoretical models.

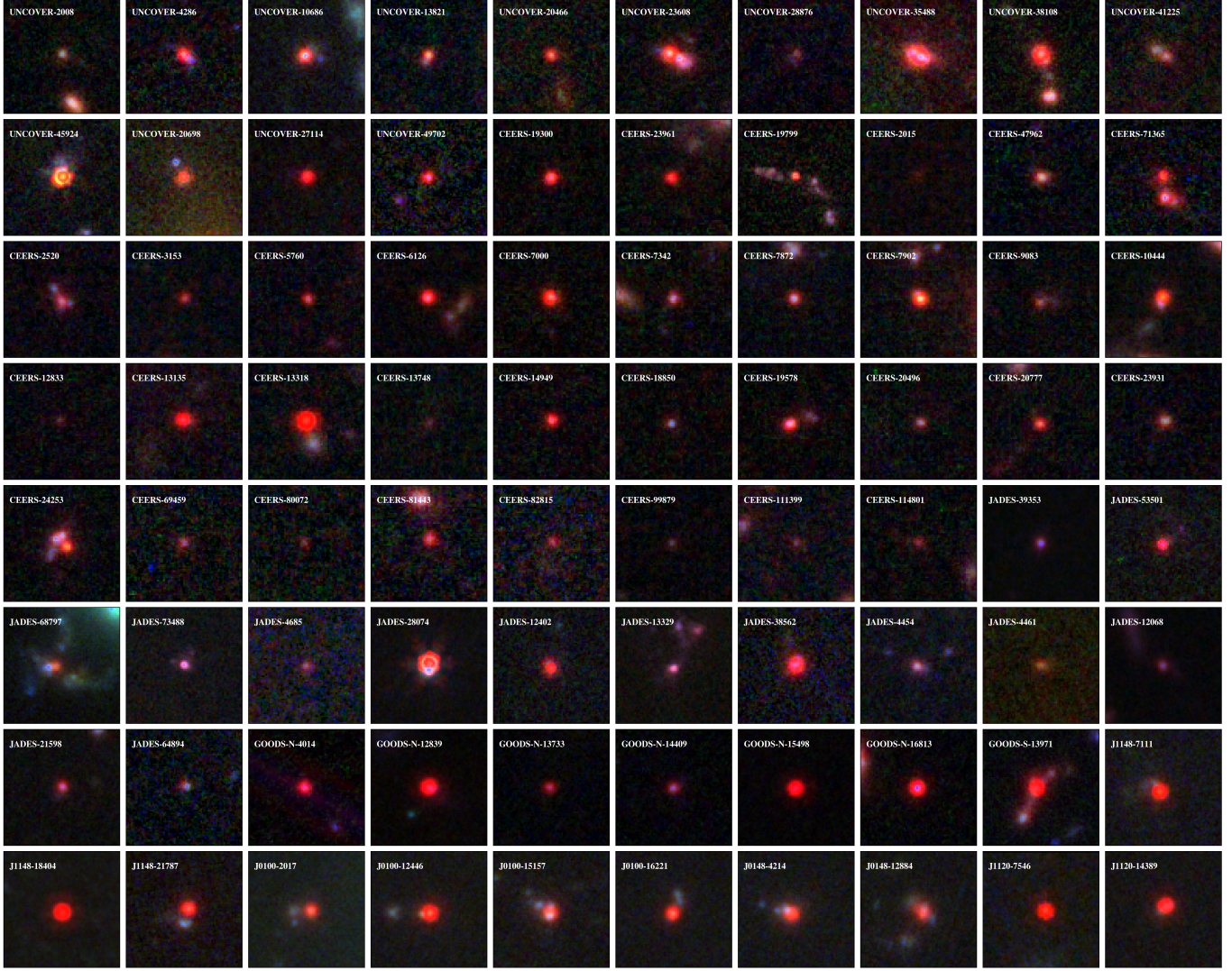
Throughout this paper, we adopt the flat Planck18 CDM cosmology (with BAO constraints, Table 2 in [Planck Collaboration VI 2020](#)), and report all magnitudes in the AB system.

2. LRD SELECTION AND DATA

2.1. LRDs from Existing JWST Catalogs

We assemble a comprehensive sample of LRDs by combining catalogs from four major independent studies:

Literature Sample



Strongly Lensed LRDs

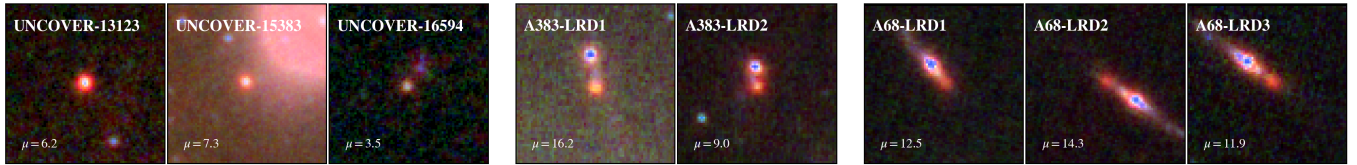
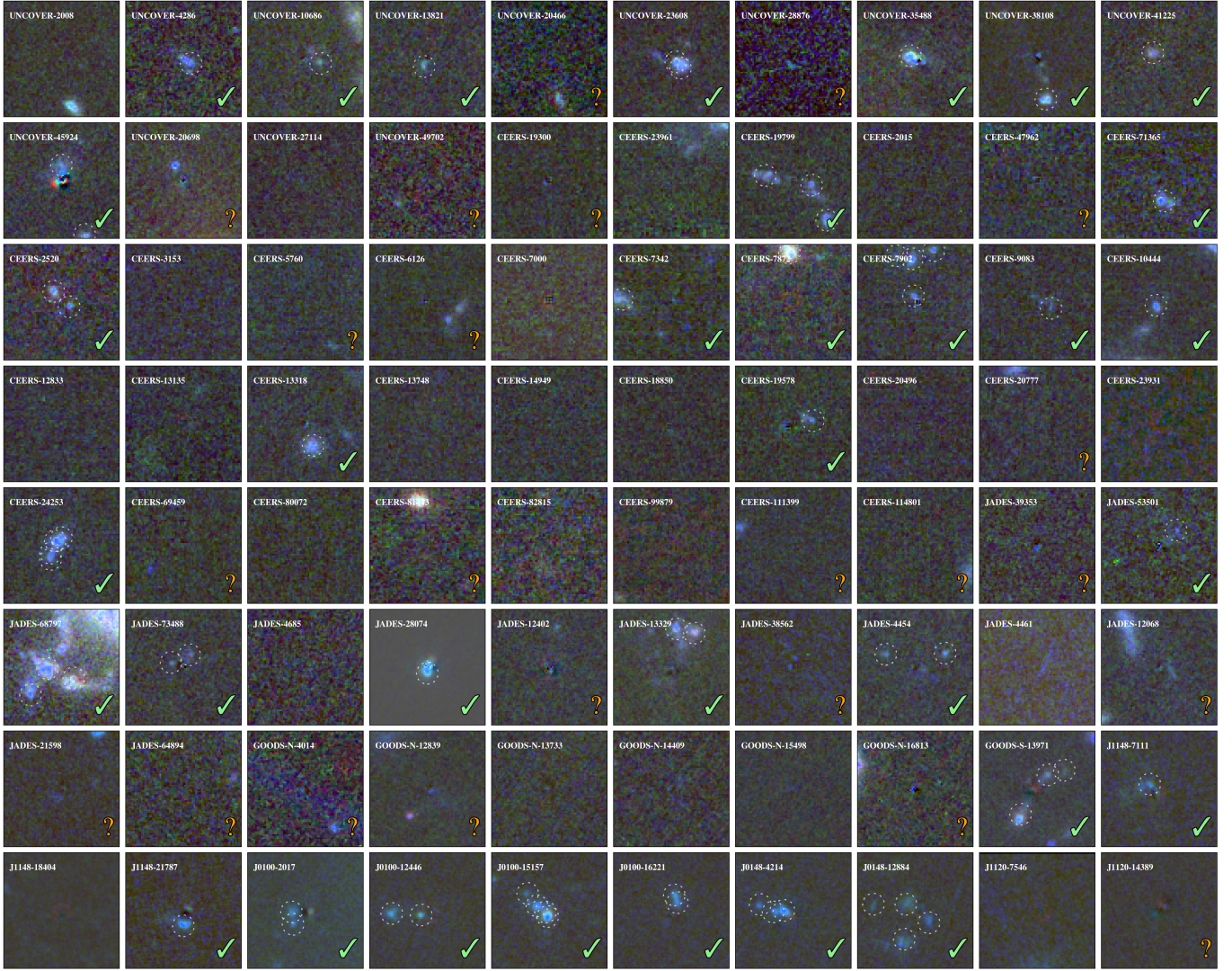


Figure 1. RGB composites of the full LRD sample. All images are $1.5'' \times 1.5''$, constructed from the available JWST/NIRCam filters for each object, selected as a function of redshift to approximately sample rest-frame UV emission (blue), wavelengths near the Balmer/4000 Å break (green), and redder rest-frame optical emission (red), depending on filter availability. For the three strongly lensed LRDs, the lensing magnifications are indicated in the lower left corner. The images are shown for illustrative purposes; all quantitative measurements are derived from the structural modeling described in Section 3.

Literature Sample



Strongly Lensed LRDs

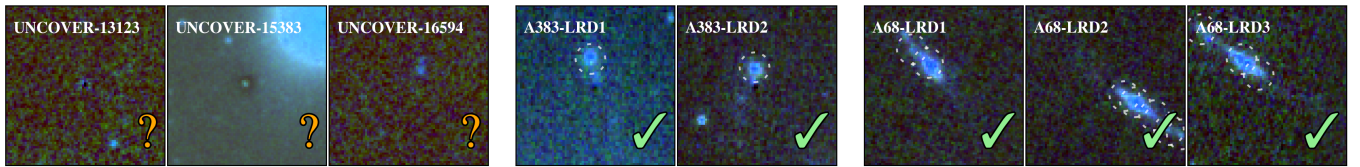


Figure 2. Same as Fig. 1, but showing residual images from the GALFIT modeling after subtracting the red component. The fits are performed in F200W and then applied to the other bands with fixed structural parameters and free magnitudes. To highlight faint UV emission, the images are displayed with a more aggressive scalings and contrast than in Fig. 1. Symbols indicate the companion classification: a checkmark (✓) denotes a robust companion, while a question mark (?) indicates a tentative candidate, identified either through a dropout consistency or the presence of faint residual emission not robustly isolated as an independent source (see Section 5.2 for details). The generally low residuals demonstrate that the F200W-based model provides a good representation of the source morphology across bands.

J. E. Greene et al. (2024), D. D. Kocevski et al. (2024), J. Matthee et al. (2024), and A. de Graaff et al. (2025b). While these catalogs rely on varying selections, the resulting compilation provides a broad and representative cross-section of the LRD population as currently defined in the literature.

To ensure reliable physical size measurements, we restrict the sample to sources with secure spectroscopic redshifts. The majority of objects in our compiled sample already have published spectra. For photometrically selected candidates from D. D. Kocevski et al. (2024), we obtain spectroscopic redshifts by cross-matching with the DAWN JWST Archive (DJA) spectroscopy table (v4.4), (using grade 2 or 3)⁴. These spectra are reduced using MSAEXP (G. Brammer 2023a), following the procedures described in A. de Graaff et al. (2024) and K. E. Heintz et al. (2024). Duplicate sources between the selections are removed by cross-matching catalogs based on sky position. To maintain a sample size manageable for detailed structural modeling, we restrict the scope of this work to LRDs selected in the Ultradeep NIRSpec and NIRCam Observations before the Epoch of Reionization (UNCOVER) program (R. Bezanson et al. 2024), the Cosmic Evolution Early Release Science (CEERS) survey (S. L. Finkelstein et al. 2023), the JWST Advanced Deep Extragalactic Survey (JADES; D. J. Eisenstein et al. 2023) complemented with the First Reionization Epoch Spectroscopically Complete Observations (FRESCO) program (PI: Oesch; PID: GO-1895 P. A. Oesch et al. 2023), and the Emission-line galaxies and Intergalactic Gas in the Epoch of Reionization (EIGER) program (PI: Lilly; PID: 1243) (D. Kashino et al. 2023).

2.2. Strongly Lensed Little Red Dots

In addition to the sample described above, we include two strongly lensed, multiply-imaged LRDs: A383-LRD and A68-LRD. A383-LRD is a striking pair of a red dot and a blue dot, embedded in a low surface brightness structure. It is described in J. F. W. Baggen et al. (2025), M. Golubchik et al. (2025), and K. K. Knudsen et al. (2025). We focus on image A383-LRD2, which lies in a cleaner background, less impacted by intracluster light, and enables detailed structural measurements (J. F. W. Baggen et al. 2025), while adopting magnification estimates from K. K. Knudsen et al. (2025) based on updated lensing models.

Motivated by the wealth of morphological information that is seen in A383-LRD on scales that are typically unresolved, we searched for additional examples of strongly-lensed LRDs. As part of this search we iden-

tify a new strongly lensed LRD, triply imaged behind the galaxy cluster Abell 68, similarly observed as part of the VENUS collaboration (Program ID: GO 6882; PI: S. Fujimoto). It is shown in the bottom panels of Fig. 1 and a larger image of the galaxy cluster with the three images is shown in the Appendix (Fig. 6). The system has a secure spectroscopic redshift from the Ly- α line (with a luminosity of $\sim 3 \times 10^{42}$ erg/s) of $z = 5.421$ (J. Richard et al. 2007) and reported magnifications for the images of $\mu_1 = 12.5 \pm 0.9$, $\mu_2 = 14.3 \pm 0.9$, and $\mu_3 = 11.9 \pm 1.1$. It has a similar morphology as A383-LRD: a close pair of compact objects, one red, one blue.

While we identified several additional candidate systems with similar morphologies, we exclude them from the analysis as they do not have spectroscopic redshifts. The status of these objects as LRDs is therefore not secure, and their physical sizes and rest-frame luminosities are uncertain. We note that one such candidate has been very recently reported in H. Yanagisawa et al. (2026), who found a star-forming clump associated with two red dots.

2.3. Imaging and Photometry

All imaging data used in this work are mosaics processed with the GRIZLI pipeline (G. Brammer 2023b), version v7.2 or later. This version includes the `snowblind` routine to mask NIRCam and NIRISS snowballs, as well as an updated bad pixel mask. Most mosaics are publicly accessible via the DJA⁵. Throughout our analysis, we require SW mosaics with 0.02''/pixel sampling and LW mosaics with 0.04''/pixel sampling.

For the UNCOVER field, we use the DR3 mosaics available through the UNCOVER data release website (K. A. Suess et al. 2024; R. Bezanson et al. 2024)⁶. These products are identical to the GRIZLI v7.2 mosaics hosted on DJA, named as `abell2744clu-grizli-v7.2-filter-clear.drc`. For the CEERS field, we use SW mosaics from DJA (v7.2), provided as 12 individual tiles, named `ceers-full-xi.yj-v7.2-filter-clear.drc`, with $i = 0-5$ and $j = 0-1$, along with LW mosaics, named `ceers-full-grizli-v7.2-filter-clear.drc`. The GOODS fields, observed through the JADES and /or FRESCO, mosaics are similarly drawn from DJA, with filenames `gds-grizli-v7.2-filter-clear.drc` and `gdn-grizli-v7.4-filter-clear.drc` for GOODS-S and GOODS-N, respectively. For the EIGER and the VENUS programs, where no public mosaics are currently available, we reduce the images locally using

⁵ <https://dawn-cph.github.io/dja/imaging/v7/>

⁶ <https://jwst-uncover.github.io/DR3.html>

⁴ <https://zenodo.org/records/15472354>

the GRIZLI v7.2 pipeline. These reductions follow the methodology outlined in the PANORAMIC field notebook⁷.

For all LRDs, we adopt published catalog photometry where available. For the UNCOVER field, we use the latest DR3 photometric catalog (R. Bezanson et al. 2024; J. R. Weaver et al. 2024; K. A. Suess et al. 2024), from which we also take the corresponding lensing magnification values. For CEERS, we use the most PR1.1 public catalog⁸. (L. Wright et al. 2024; J. R. Weaver et al. 2024). For sources in JADES and/or FRESCO, photometry is taken from the v2.0 and v1.0 public catalogs (M. J. Rieke et al. 2023).⁹ The photometry for the LRDs detected with the EIGER program is reported in Appendix A. Table 8 in J. Matthee et al. (2024); the methodology is reported in D. Kashino et al. (2023).

For the newly identified systems presented in this work, we perform our own multi-band photometric measurements following the procedure described in J. F. W. Baggen et al. (2025). In short, we perform PSF-matched aperture photometry using 0.5'' circular apertures. All JWST images are convolved to match the F444W PSF, and we apply aperture corrections to both the measured fluxes and uncertainties, which are derived empirically from source-free background regions.

We emphasize that the photometry is used primarily to measure total fluxes and luminosities of the LRDs, and not as the basis for the component-resolved structural analysis, which relies on direct image modeling.

Using the imaging products, we exclude 14 LRDs from the parent sample that lack coverage in the key bands required for this analysis. All retained sources therefore have consistent multi-band imaging suitable for reliable morphological and photometric measurements.

The final sample consists of 83 LRDs. For consistency, we adopt the source identifiers assigned in the original works from which the LRDs were selected. The sample includes three strongly lensed LRDs: the triply imaged LRD in Abell 2744 (UNCOVER-13123, UNCOVER-15383, and UNCOVER-16594), the double imaged LRD in Abell 383 (A383-LRD1 and A383-LRD2), and the triply imaged in Abell 68 (discovered in this work, named A68-LRD1, A68-LRD2, A68-LRD3). Each strongly lensed system is counted only once in the total sample size. For the analysis pre-

sented here, we focus on a single representative image for each system—UNCOVER-16594, A383-LRD2, and A68-LRD1 to avoid double counting. Figure 1 shows RGB image stamps of all sources included in the analysis.

3. STRUCTURAL MODELING AND SPECTRAL ENERGY DECOMPOSITION

In this section, we describe how we identify distinct structural components associated with each LRD, measure their projected separations, and extract component-resolved spectral energy distributions. These measurements form the basis for estimating the local ultraviolet radiation field in the following section.

3.1. Component Identification

Using all available imaging, we investigate whether LRDs consist of a single compact source or contain physically distinct components at small projected separations. We developed a source-finding pipeline that identifies such components in two stages.

First, we generate a segmentation mask for the 1.5'' cutout using standard `photutils` detection (L. Bradley et al. 2025) on a high-SNR stack of all available bands. This reliably identifies the primary red dot and any clearly separated neighbors. However, the resulting mask for the central LRD is often quite large, potentially obscuring companions that are distinct in the higher-resolution UV bands and very close but blended at longer wavelengths.

To recover this substructure, we perform a second step by using only the short-wavelength bands (F070W–F150W). We make a new segmentation mask, allowing lower SNR ratio > 3 , and separated from the red centroid by at least 1 pixel. This approach allows us to robustly identify single compact companions, multiple knots, or faint extended emission next to the compact red dot that would otherwise be lost within the central mask.

Once components are identified, we assess their physical association with the LRD. For blue knots recovered directly within the central mask (via the second step), the projected separation is extremely small. We therefore assume these are intrinsic parts of the LRD system. This interpretation is further supported by the frequent presence of extended emission aligned with the same direction in the full multi-band images, as well as by visual confirmation that these components exhibit consistent dropout signatures, with vanishing flux shortward of the Lyman limit.

For more distant neighbors outside the central mask, we rely on photometric redshifts derived using `EAZY`

⁷ <https://github.com/gbrammer/panoramic-jwst/blob/main/Notebooks/step3-panoramic-mosaics.ipynb>

⁸ <https://zenodo.org/records/11658282>

⁹ <https://archive.stsci.edu/hlsp/jades>; Newer versions have since become available; however, the catalog adopted here was the latest public release at the time the majority of this analysis was performed.

ID	RA	DEC	z	μ	N_{comp}	d_{eff} [pc]	$M_{\text{UV,tot}}$	$M_{\text{LW,tot}}$	$\log_{10}(J_{21})$
A68-LRD1	9.26778	9.16196	5.42	12.5	2	0.40	-19.0	-18.5	4.7
A383-LRD2	42.01924	-3.53292	6.03	9.0	1	0.34	-18.1	-17.5	4.4
UNCOVER-4286	3.61920	-30.42327	5.84	1.6	1	0.37	-18.5	-18.0	4.5
UNCOVER-10686	3.55084	-30.40660	5.05	1.4	1	0.82	-17.8	-17.1	3.5
UNCOVER-13821	3.62061	-30.39995	6.34	1.6	1	0.44	-16.2	-15.3	3.3
UNCOVER-23608	3.54282	-30.38065	5.80	2.1	2	0.79	-18.6	-17.9	3.8
UNCOVER-35488	3.57898	-30.36260	6.26	3.4	1	0.31	-18.1	-16.9	4.2
UNCOVER-38108	3.53001	-30.35801	4.96	1.6	1	2.80	-18.4	-17.9	2.7
UNCOVER-41225	3.53399	-30.35331	6.76	1.5	1	0.68	-18.2	-17.7	3.9
UNCOVER-45924	3.58476	-30.34363	4.46	1.6	2	0.61	-19.1	-18.6	4.3
CEERS-19799	214.92415	52.84905	4.22	-	3	2.42	-20.2	-19.7	3.6
CEERS-71365	214.89554	52.90672	4.80	-	1	1.75	-19.4	-19.0	3.6
CEERS-2520	214.84477	52.89210	8.69	-	2	0.74	-19.5	-19.0	4.3
CEERS-7342	215.00849	52.97797	6.12	-	1	3.96	-20.5	-20.0	3.3
CEERS-7872	214.87615	52.88083	8.36	-	1	3.04	-20.8	-20.4	3.6
CEERS-7902	214.98304	52.95601	6.99	-	4	0.87	-20.2	-19.7	4.5
CEERS-9083	214.79753	52.81876	6.62	-	1	0.87	-18.6	-18.1	3.8
CEERS-10444	214.89225	52.87741	6.69	-	1	0.52	-19.1	-18.7	4.5
CEERS-13318	214.79537	52.78885	5.28	-	1	1.89	-19.9	-19.4	3.7
CEERS-19578	214.88016	52.81256	5.28	-	1	1.71	-18.5	-18.0	3.2
CEERS-24253	214.97996	52.86108	6.23	-	4	1.01	-20.4	-19.9	4.4
JADES-53501	189.29506	62.19357	3.44	-	1	2.25	-17.4	-16.9	2.5
JADES-68797	189.22914	62.14619	5.04	-	3	0.72	-20.4	-19.6	4.6
JADES-73488	189.19740	62.17723	4.13	-	2	1.07	-17.2	-16.7	3.1
JADES-28074	189.06459	62.27382	2.27	-	1	0.30	-19.6	-18.8	5.0
JADES-13329	53.13904	-27.78443	3.94	-	2	3.95	-19.0	-18.4	2.6
JADES-4454	53.16611	-27.77204	6.30	-	2	2.46	-17.5	-17.0	2.5
GOODS-S-13971	53.13858	-27.79025	5.48	-	3	2.21	-19.7	-19.2	3.5
J1148-7111	177.10171	52.90796	4.34	-	1	0.93	-19.6	-19.2	4.2
J1148-21787	177.02142	52.83362	4.28	-	1	1.23	-19.3	-18.9	3.8
J0100-2017	15.05804	28.07241	4.94	-	2	1.49	-17.6	-17.1	3.0
J0100-12446	15.04825	28.00972	4.70	-	2	1.49	-19.5	-18.9	3.7
J0100-15157	15.03025	28.05018	4.94	-	4	0.86	-20.6	-20.1	4.6
J0100-16221	15.03404	28.05158	4.35	-	2	1.40	-19.1	-18.7	3.6
J0148-4214	27.13871	5.99723	5.02	-	3	0.53	-20.1	-19.7	4.9
J0148-12884	27.17325	6.01592	4.60	-	4	1.77	-20.1	-19.6	3.8

Table 1. Physical properties of LRD systems with candidate companions ($N_{\text{comp}} \geq 1$). Listed are the source coordinates, spectroscopic redshift, lensing magnification μ , and the number of companion components identified by our source-finding pipeline within a $1.5''$ cutout (see Section 3.1). The effective separation d_{eff} corresponds to the projected distance at which a single companion with the same total LW luminosity would reproduce the combined LW radiation field from all companions (see Section 4). $M_{\text{LW,tot}}$ denotes the total intrinsic luminosity of the companion population integrated over the Lyman–Werner band (91.2–111 nm), computed from the intrinsic SED templates, while $M_{\text{UV,tot}}$ is the corresponding rest-frame 1500Å absolute magnitude. The final column reports the resulting incident LW intensity at the position of the compact red component, expressed as $J_{21,\text{LW}}$ (computed from $M_{\text{LW,tot}}$ and d_{eff}). * This source has additional confirmed companions (A. Torralba et al. 2026); here we report only the two companions as found within the $1.5''$ cutout.

(G. B. Brammer et al. 2008) to rule out chance projections. We first perform unconstrained free-redshift fits. For sources with broad filter coverage, these fits often converge robustly. For example the outer knot in the bottom of UNCOVER-45924 converges to $z = 4.46$. Notably, this companion has since been spectroscopically confirmed by A. Torralba et al. (2026), who also identify additional companions at larger projected separations, lending confidence to both our source detection and photometric-redshift methodology. However, for fainter sources or those lacking strong dropout constraints, the free-redshift solutions can be poorly constrained. In such cases, we perform a second fit with the redshift fixed to the LRD spectroscopic redshift, z_{spec} . A neighbor is classified as a companion if the fixed-redshift fit is statistically consistent with the data, defined by $\chi^2(z_{\text{spec}}) - \chi^2(z_{\text{free}}) < 1$. For these systems, the physical association remains less secure and should be interpreted with caution until spectroscopic confirmation becomes available.

For the triply imaged system in Abell 2744, the interpretation of companions requires additional care. While companions are identified for the images UNCOVER-13123 and UNCOVER-16594, no companion is detected for UNCOVER-15383, and the properties of the candidate companions differ between the images. We therefore treat these companions as tentative. Further confirmation will require a detailed delensing analysis to the source plane and consistency checks across all multiple images.

In total, 36 LRDs (43% of the sample) show evidence for at least one physically associated companion ($N_{\text{comp}} \geq 1$). For these systems, the identified companions are encircled in Fig. 2, which shows residual images from the GALFIT modeling after subtraction of the red component (see the following section for details). This component identification step defines the set of UV sources used to estimate the local Lyman-Werner radiation fields, which we quantify in the following sections. Systems with $N_{\text{comp}} \geq 1$ are summarized in Table 1, while LRDs without identified companions are listed in the Appendix.

3.2. Sérsic Profile Fitting

To measure the projected separations between the compact red component and any associated companions, we model the surface brightness distributions of the systems using two-dimensional Sérsic profile fitting with GALFIT (C. Y. Peng et al. 2002, 2010). Structural modeling is performed in the F200W band, which provides the highest signal-to-noise ratio at optimal an-

gular resolution. For a small number of sources without F200W coverage, we instead use the F210M image.

We model each system using a multi-component Sérsic fit consisting of the central red dot and its associated companion(s), as identified by our initial source-finding pipeline. The number of fitted components is therefore $N_{\text{fit}} = N_{\text{comp}} + 1$, where N_{comp} the number of companions and the additional component corresponds to the red dot itself. For each component, we optimize the centroid position (x, y) , effective radius (r_e), integrated magnitude, axis ratio (b/a), and position angle (PA). Initial centroid positions are taken from the pipeline but are allowed to vary freely during the fitting. To ensure stability in the multi-component fits, we fix the Sérsic index to $n = 1.5$ for all components. Parameter ranges are restricted to $r_e = 0.5\text{--}50$ pixels, $b/a = 0.1\text{--}1.0$, and magnitudes between 1 and 100. For the compact red component, we further restrict the effective radius to $r_e \leq 10$ pixels, given its compact nature. For the strongly lensed, triply imaged system A68-LRD, we impose additional constraints to avoid unphysical solutions driven by lensing distortions. In this case, the centroid position of the red component is fixed during the fit and set to the position of the red emission identified by the source-finding pipeline. We also require $b/a > 0.5$ to prevent the model from converging to highly elongated profiles. These constraints are motivated by the observed morphology of the red component, which appears compact and spheroidal in the long-wavelength NIRCam bands. Prior to fitting, we use sigma-clipped background statistics to identify and mask contaminating foreground or background sources. From this mask, we then ensure that any potential companion is excluded.

For the lensed systems (UNCOVER sources, A383-LRD, and A68-LRD) we apply magnification corrections to all measured physical quantities. The adopted magnification values (μ) are listed in Table 1. For projected separations between components, we divide the observed distances by $\sqrt{\mu}$. However, in several strongly lensed cases, most notably A68-LRD, the separation direction lies approximately along the arc, and may therefore be closer to the total magnification. In such cases, the true separations could be smaller than assumed, and the corresponding radiation field (which scales as $1/d^2$) would be correspondingly stronger. Observed fluxes are divided by μ .

This procedure yields a consistent set of component centroids and projected separations for all systems, which we use in the analysis that follows.

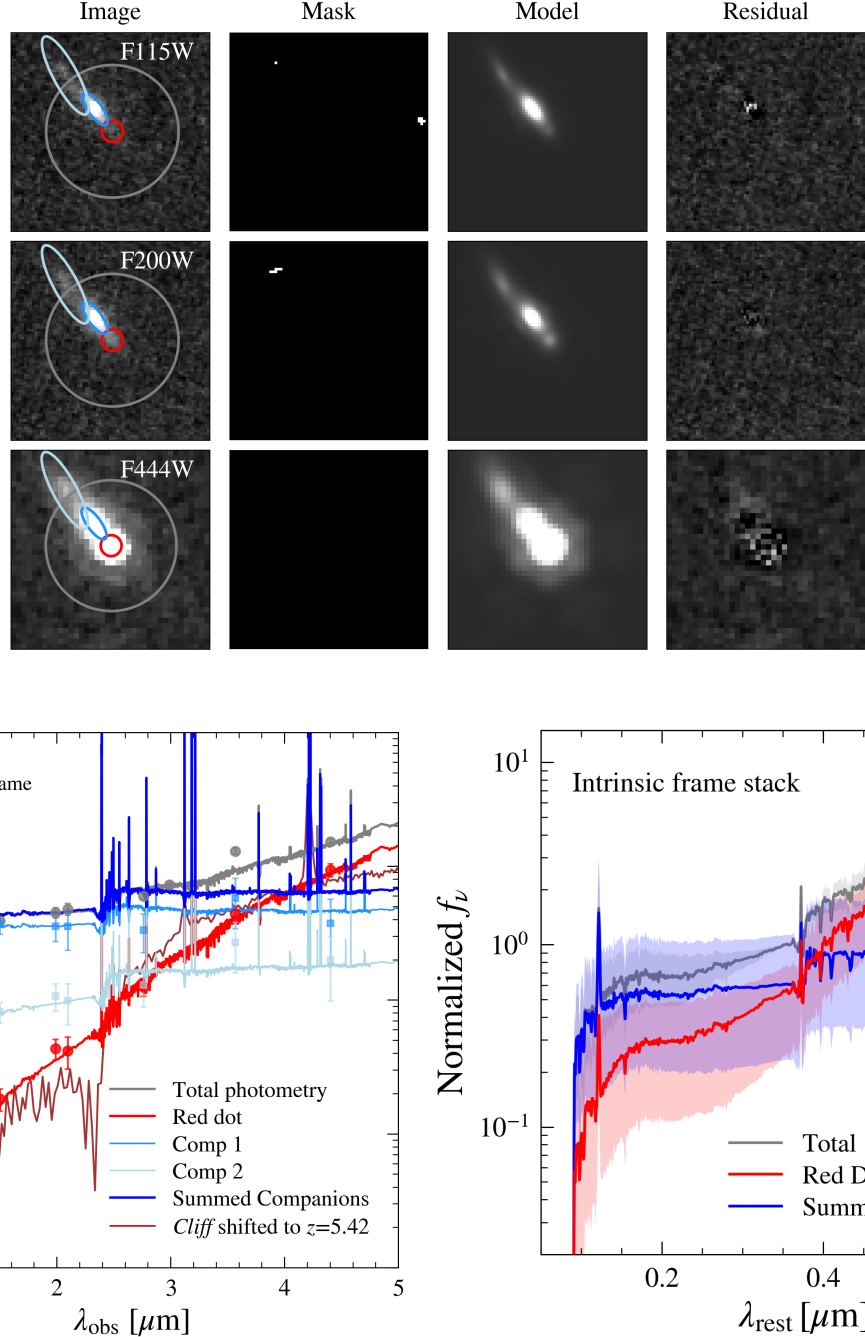


Figure 3. *Top:* JWST/NIRCam cutouts in three filters (F115W, F200W, F444W), the corresponding segmentation mask, best-fit GALFIT model, and residual image for A68-LRD1. Ellipses indicate the fitted component parameters from F200W, overlaid on all bands. The gray circle shows the 0.5'' photometric aperture. *Bottom left:* SED decomposition for A68-LRD1. Gray points show the observed total (observed) aperture photometry, while the red and blue points show the forced photometry obtained from the GALFIT fits shown in the top panel, adopting the same color scheme. Solid curves show the best-fit EAZY templates. These SEDs are shown in the observed frame, meaning that they include lensing magnification and IGM absorption. Overplotted is the *Cliff* spectrum from A. de Graaff et al. (2025a), only corrected for the redshift difference (without any renormalization), showing remarkable resemblance to the SED shape *and* intrinsic luminosity. *Bottom right:* Stacked intrinsic rest-frame SEDs for all LRDs with companions. For each system, the total SED (gray) is normalized to the total flux density at a rest-frame wavelength of $0.3645\mu\text{m}$ (Balmer break). The red and blue component SEDs are shown relative to this normalization. Shaded regions indicate object-to-object scatter (16th–84th percentile). For systems with multiple companions, the blue curve represents the sum of all companions.

3.3. Forced Photometry and Component SEDs

Having identified the relevant components and measured their projected separations, we next determine the ultraviolet emission associated with the compact red source and any nearby companions.

Using the fit in F200W/F210M, we then perform forced photometry on the remaining bands to disentangle the spectral energy distributions of the components, following the methodology of [J. F. W. Baggen et al. \(2025\)](#). We fix all structural parameters ($x, y, r_e, n, b/a, \text{PA}$) to the values determined from the initial fit and allow only the magnitude to vary. This ensures that flux is extracted from consistent physical regions across all filters, allowing us to robustly "split" the SEDs of the red dot and offset emission. Ideally, such decomposition would be achieved through spatially resolved spectroscopy. In the absence of such data, forced multi-band photometry provides a valuable tool to isolate the light of the individual components using the available imaging.

Figure 3 illustrates this procedure for A68-LRD1. The left panel shows the F115W, F200W, and F444W cutouts alongside the segmentation mask, model, and residuals. The ellipses indicate the (fixed) positions, sizes, and orientations of the fitted components derived from F200W and overlaid on all bands. The gray circle is shown to highlight the 0.5'' aperture used to measure the total photometry. The forced photometry produces remarkably stable fits across all filters despite the fixed geometry.

The middle panel shows the observed-frame SED decomposition for the same system. The grey points and corresponding solid curve represent the total aperture photometry and the associated best-fit EAZY template. To isolate the distinct physical contributions within the system, we plot the forced photometry for the individual components as colored points, with the solid curves the corresponding best-fit EAZY templates. The red component exhibits an extremely steep red spectrum, closely resembling the spectral shape reported for the *Cliff*-LRD ([A. de Graaff et al. 2025a](#)) (overplotted). This spectrum is corrected only for the redshift difference, without any renormalization, and therefore matches not only the spectral shape but also the intrinsic luminosity. While EAZY interprets the red component as a smooth continuum from a stellar population and does not capture the extreme Balmer absorption, the close resemblance nonetheless highlights the diagnostic power of strong lensing, which allows the light from the system to be spatially separated and analyzed in detail, even using photometry alone.

This decomposition enables us to quantify the relative contributions of the compact red source and the nearby companions across wavelength. We perform this SED decomposition for all systems, shift each to the rest frame, and normalize by the total SED flux at the Balmer break (rest-frame 0.3645 μm), as shown in the right panel. We interpolate each component's template onto a common logarithmic rest-frame wavelength grid spanning 0.05–0.7 μm with 800 points. The shaded regions present the 16th–84th percentile range computed at each wavelength across the sample. The solid curves show the median of the distribution. For LRDs with more than one companion, the blue curve represents the sum. The stacked rest-frame SEDs reveal a consistent picture: the red components dominate at $\lambda_{\text{rest}} \gtrsim 0.4 \mu\text{m}$ with steeply rising continua, while the companions contribute primarily at UV wavelengths ($\lambda_{\text{rest}} \lesssim 0.3 \mu\text{m}$) with relatively flat spectra. The companions are therefore best interpreted as young, star-forming systems with modest stellar masses (typically of order $\sim 10^8\text{--}10^9 M_\odot$, with a mean for the total sample of $\langle \log(M_*/M_\odot) \rangle = 8.8$). Some individual cases can reach higher inferred stellar masses, such as UNCOVER-45924 ("Monster" LRD), with a stellar mass of $\sim 10^{10.2} M_\odot$, despite separating the UV emission from the red component. This remains lower than the mass inferred when the full SED, including the Balmer break, is fit ($\sim 10^{10.9} M_\odot$ [I. Labbe et al. 2024](#)). Another massive example is JADES-68797, with $M_* \sim 10^{10.5} M_\odot$.

We note that the stacked red-component SED is generally less steep than the individual strongly lensed cases (which are more comparable to the *Cliff*). This likely reflects residual blending with surrounding stellar light, either from the host galaxy or nearby companions (see Discussion Section 5.1), which is difficult to fully remove in unlensed systems.

Together, the SEDs from the companions and projected separations derived here provide the observational inputs required to estimate the local LW radiation field experienced by the compact red components, which we quantify in the next section.

4. LYMAN-WERNER RADIATION FROM THE COMPANIONS

We now estimate the Lyman–Werner (LW) radiation field at the position of the red component. For each companion i , we take the best-fit SED template obtained through the forced multi-band photometric decomposition (Section 3.3). In the EAZY fitting, we disable intergalactic medium absorption, such that the templates represent the emitted UV spectrum rather than the attenuated observed flux. From this, we compute the

mean flux density in the rest-frame LW band, defined as 91.2–111 nm, and convert it to an intrinsic LW luminosity, using the luminosity distance at the source redshift:

$$L_{\nu,i}^{\text{LW}} = \frac{4\pi d_L^2}{1+z} \langle f_{\nu,i} \rangle_{\text{LW}}. \quad (1)$$

By assuming isotropic emission from each companion and dilution over the projected separation (d_i), we obtain the LW radiation field at the position of the red component:

$$J_{\nu} = \frac{1}{4\pi} \sum_i \frac{L_{\nu,i}^{\text{LW}}}{4\pi d_i^2}, \quad (2)$$

which is often expressed in dimensionless form as

$$J_{21,\text{LW}} \equiv \frac{J_{\nu}}{10^{-21} \text{ erg s}^{-1} \text{ cm}^{-2} \text{ Hz}^{-1} \text{ sr}^{-1}}. \quad (3)$$

For convenience, we define the total LW specific luminosity of all companions (if more than one) as

$$L_{\nu,\text{LW}}^{\text{tot}} = \sum_i L_{\nu,i}^{\text{LW}}, \quad (4)$$

and an effective separation d_{eff} such that

$$\frac{L_{\nu,\text{LW}}^{\text{tot}}}{d_{\text{eff}}^2} = \sum_i \frac{L_{\nu,i}^{\text{LW}}}{d_i^2}. \quad (5)$$

By construction, the LW radiation field computed from $(L_{\nu,\text{LW}}^{\text{tot}}, d_{\text{eff}})$ is identical to that obtained by summing the contributions of individual companions. This reparameterization allows us to compare LRDs that have different numbers of companions in a consistent way.

For comparison with more commonly used UV diagnostics, we also measure the total intrinsic rest-frame UV magnitude at 1500 Å, $M_{\text{UV,tot}}$, computed from the same intrinsic SED templates. All derived quantities, including projected separations, $M_{\text{UV,tot}}$, $M_{\text{LW,tot}}$, and the inferred $J_{21,\text{LW}}$, are reported in Table 1.

Figure 4 shows the companion LW magnitude ($M_{\text{LW,tot}}$) as a function of separation d_{eff} . The diagonal contours indicate constant $J_{21,\text{LW}}$, illustrating that sources of different luminosities can generate comparable radiation fields depending on their distance to the red component.

Across the sample, we infer LW radiation fields of $J_{21,\text{LW}} \sim 10^{2.5-5}$, with most LRDs exceeding commonly adopted thresholds for fragmentation suppression ($J_{\text{crit}} \sim 10^3$). These radiation fields place the red components in a regime where molecular hydrogen cooling is expected to be strongly suppressed, allowing the gas to approach the atomic-cooling limit without fragmentation and star formation (Z. Haiman et al. 1997; M. Dijkstra et al. 2008; M. Dijkstra et al. 2014).

For the minority of LRDs with inferred LW radiation fields just below the canonical threshold, the same formation pathway may still apply. The commonly quoted value ($J_{\text{crit}} \sim 10^3$) should not be interpreted as a sharp limit. Additional processes, such as dynamical heating during halo mergers (N. Yoshida et al. 2003; J. H. Wise et al. 2019) or the presence of baryonic streaming velocities (T. H. Greif et al. 2011; M. A. Latif et al. 2014), can further suppress fragmentation and delay star formation prior to reaching the atomic-cooling regime. Moreover, the companions may have been brighter or at smaller separations in the past, implying higher LW intensities than those inferred at the epoch of observation.

The above estimates for the LW radiation field do not account for self-shielding effects (J. Wolcott-Green et al. 2017) due to a column of gas between the blue and red components. We test whether this affects our conclusions by estimating the timescale for molecular hydrogen dissociation in this column. For a red component exposed to an intrinsic LW radiation field $J_{21,\text{LW}}$ produced by its companion(s), the corresponding LW photon production rate of the companions can be written as $\dot{N}_{\text{LW}} = 3.5 \times 10^{48} (4\pi)(d_{\text{eff}}/\text{kpc})^2 J_{21,\text{LW}}$ photons s⁻¹. Assuming the LW photons dissociate H₂ with 10% efficiency, we can estimate the propagation of the H₂ dissociation front through a sphere with radius d_{eff} , following equation (2) of J. Sullivan et al. (2025), as

$$4\pi R^2 n_{\text{H}_2} dR = (0.1 \dot{N}_{\text{LW}} - 4\pi k_9 \int n_{\text{H}} n_{\text{e}} r^2 dr) dt, \quad (6)$$

with k_9 , the H₂ formation rate, given in Table (A1) of S. P. Oh & Z. Haiman (2002). Following the model used in M. T. Scoggins & Z. Haiman (2024), we estimate n_{H} assuming the primordial gas is initially compressing adiabatically, giving a maximum central number density $n_{\text{c}} \sim 6(T_{\text{vir}}/1000\text{K})^{3/2} \text{ cm}^{-3}$ (E. Visbal et al. 2014) and residual electron fraction $n_{\text{e}}/n_{\text{H}} = 1.2 \times 10^{-5} \sqrt{\Omega}/(\Omega_{\text{b}} h)$ (P. J. E. Peebles 1993). We approximate the H₂ abundance using equation (3) of M. T. Scoggins & Z. Haiman (2024). We assume that the gas that hosts the red component has not begun fragmentation and is approaching the atomic cooling limit, with $T \sim 8000\text{K}$, and is experiencing a faint background LW radiation $J_{21,\text{LW}} = 0.1 J_{21}$.

Once the blue companion turns on, the gas out to the red component is irradiated by an LW field $J_{21,\text{LW}} \gtrsim J_{\text{crit}}$. We find that for a representative separation of $d_{\text{eff}} = 1 \text{ kpc}$, molecular hydrogen is fully dissociated within $\sim 10,000 \text{ yr}$. We conclude that self-shielding effects likely become negligible by the time the red clump begins its collapse, since the dynamical timescales are much longer than this H₂ dissociation timescale.

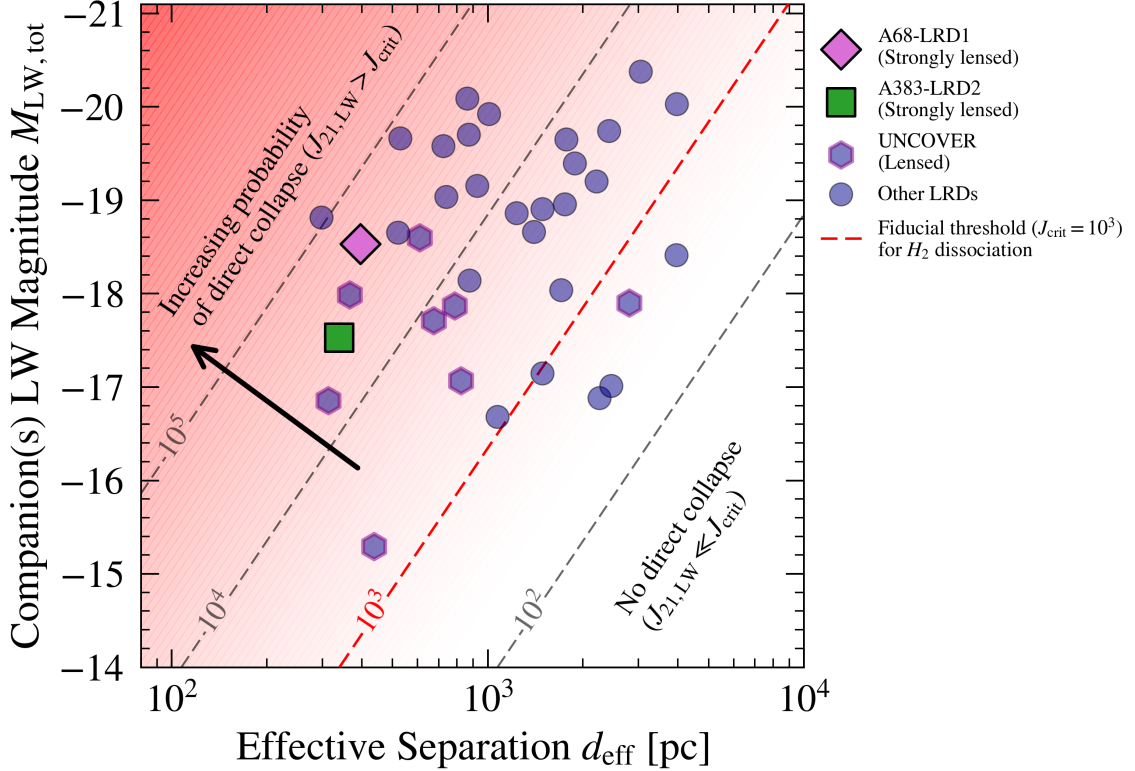


Figure 4. The total LW magnitude of the companion(s), $M_{\text{LW,tot}}$, is shown as a function of the effective projected separation from the compact red component, d_{eff} (defined such that $L_{\text{LW,tot}}/d_{\text{eff}}^2 = \sum_i L_{\text{LW},i}/d_i^2$ when an LRD has multiple companions). Diagonal lines indicate constant LW radiation intensity, $J_{21,\text{LW}}$, incident on the red component. Systems toward the upper left correspond to brighter companions at smaller separations and therefore higher LW intensities. The red dashed line marks a commonly adopted critical threshold for molecular hydrogen dissociation ($J_{\text{crit}} = 10^3$), above which fragmentation is expected to be strongly suppressed. Shaded regions illustrate increasing likelihood for collapse in an LW-regulated regime.

5. DISCUSSION

5.1. A Concordance Picture for LRDs: Direct Collapse Induced by Intense Lyman-Werner Radiation

A substantial fraction of Little Red Dots (43%) are found in close proximity to one or more UV-bright companions. Using component-resolved photometry and projected separations, we show that these companions generate intense local Lyman-Werner radiation fields at the locations of the compact red components, with inferred intensities of $J_{21,\text{LW}} \sim 10^{2.5}-10^5$. These values are comparable to, and often significantly exceed, commonly adopted thresholds required to suppress molecular hydrogen cooling and fragmentation.

The frequent occurrence of such configurations (see also J.-T. Schindler et al. 2025; A. Torralba et al. 2026; R. M. Mérida et al. 2025; P. Rinaldi et al. 2024; C.-H. Chen et al. 2025; T. S. Tanaka et al. 2024; H. Yanagisawa et al. 2026; F. D'Eugenio et al. 2026), strongly suggests that this is not incidental, but instead reflects a necessary environmental condition for the formation of LRDs. In this picture, intense local LW radiation

suppresses molecular cooling in a nearby atomic-cooling halo, preventing fragmentation and enabling rapid collapse to high densities. The immediate products of such collapse are expected to be accretion-dominated configurations, producing supermassive stars or quasi-star-like structures (if there is a pre-existing stellar-mass black hole embedded in the pristine cloud), often referred to as “direct-collapse” scenarios. If fragmentation is delayed but not entirely suppressed, the same collapse process can also yield extremely dense stellar systems, providing another potential pathway toward massive black hole formation (see references in the Introduction). The relative importance of these outcomes depends on metal enrichment, gas inflow rates, angular momentum transport, and small-scale fragmentation physics (e.g., M. Volonteri 2010; K. Omukai et al. 2008; B. Devecchi & M. Volonteri 2009; K. Inayoshi & Z. Haiman 2014; M. A. Latif et al. 2016; J. A. Regan & M. G. Haehnelt 2009; S. Chon & K. Omukai 2020, 2025).

This framework naturally promptly produces a massive (up to 10^6 M_\odot) black hole, still surrounded by its extremely dense natal cloud, which connects several

otherwise puzzling observational properties of LRDs. The extreme compactness of the red components follows directly from collapse in an LW-regulated regime, in which gas approaches the atomic-cooling limit without fragmenting into a normal stellar population. It also explains the extremely steep, in some cases nearly blackbody-like, rest-frame optical continua, with Balmer breaks, Balmer absorption and exponential wings, observed in many systems. These have been attributed to accreting black holes embedded in dense, optically thick gas configurations, variously described as cocoons, or envelopes (sometimes phenomenologically dubbed BH*) (K. Inayoshi & R. Maiolino 2025; X. Ji et al. 2025; F. D’Eugenio et al. 2025a; I. Juodžbalis et al. 2024; R. P. Naidu et al. 2025; A. Sneppen et al. 2026; A. de Graaff et al. 2025a,b; V. Rusakov et al. 2025; H. Liu et al. 2025; D. Kido et al. 2025). In a LW-regulated collapse scenario, the collapse itself can naturally generate a gas compaction event (E. Cenci & M. Habouzit 2025), reproducing the observed spectra of LRDs, while also providing a plausible explanation for the observed X-ray weakness (e.g. T. T. Ananna et al. 2024). Such spectra have additionally been shown to be consistent with predictions from MESA-based stellar evolution models of quasi-stars, which naturally reproduce the observed SEDs (A. D. Santarelli et al. 2025a).

In addition, it provides a natural explanation for the characteristic V-shaped SEDs seen in the integrated light of many LRDs. In this picture, the V-shape arises from the superposition of the compact red component and nearby UV-bright companions, as directly demonstrated by strongly lensed, spatially resolved systems (J. F. W. Baggen et al. 2025) (and see Figure 3). Without the aid of strong lensing, such configurations generally remain unresolved at JWST resolution, causing the combined emission to appear as a single compact source with distinctive colors. In hindsight, the commonly used photometric selection of LRDs has proven highly effective at identifying candidate collapse systems, as it implicitly selects objects in which compact red components are in very close proximity to UV-bright companions, thereby explaining why the joint requirement of compactness and V-shaped colors always selects broad-line sources (R. E. Hviding et al. 2025).

From a complementary perspective, W. Q. Sun et al. (2026) interpret LRDs as systems consisting BH*’s embedded within a surrounding host galaxy, based on fits to their integrated spectral emission. Our results provide a morphological basis for this interpretation by demonstrating that the red and blue components are often spatially distinct, and that the steep red continuum (BH*-like) can be isolated from surrounding star-

forming emission. From our component-resolved SED fitting, we find that the companions typically have modest stellar masses of order $M_\star \sim 10^8\text{--}10^9 M_\odot$, consistent with the stellar masses inferred from narrow emission lines (e.g., F. D’Eugenio et al. 2025b, 2026; W. Q. Sun et al. 2026; X. Ji et al. 2025; A. Torralba et al. 2025).

Finally, as a natural consequence of this picture, LRDs need not represent a single, discrete class of objects. In LW-regulated environments, the initial collapse sets the conditions for highly compact systems, while the precise outcome and observable appearance may depend on evolutionary stage (see also Section 5.3). Depending on timing and sub-sequent star formation or accretion, such systems may be observed as supermassive stars or quasi-star-like phases, extremely compact stellar systems, or accretion-dominated sources. In this sense, LRDs may trace a continuous sequence in which the relative contributions of accretion-powered emission and stellar light vary (e.g., P. G. Pérez-González et al. 2024; G. Barro et al. 2025, 2026; G. C. K. Leung et al. 2025; W. Q. Sun et al. 2026; D. Herrero-Carrión et al. 2025; P. Natarajan et al. 2017; see also Billand et al., in prep.). We therefore do not claim any unique physical interpretation of LRDs here, but emphasize that many of the proposed natures for LRDs (L. Zwick et al. 2025; F. Pacucci et al. 2026; E. Cenci & M. Habouzit 2025; J. Jeon et al. 2025; Q. Fei et al. 2025; A. D. Santarelli et al. 2025b; M. C. Begelman & J. Dexter 2025), require fragmentation to be strongly suppressed and are compatible with the intense local LW radiation fields inferred here.

5.2. Frequency of UV-Bright Companions

A strong prediction of this scenario is that every LRD has, or had at some point in its evolution, a companion object whose LW radiation exceeds the limit for H₂ dissociation. The observed fraction is high but not 100% (see Section 3.1), seemingly in conflict with this expectation. However, the true fraction is almost certainly significantly higher than our reported fraction.

First, our search is intentionally conservative, using 1.5'' cutouts and thus effectively focusing on companions $\sim 0.75''$ away from the compact red component. At the average redshift of the sample ($z = 5.6$), this corresponds to a projected physical scale of ~ 4.5 kpc. As illustrated in Fig. 5, for systems classified as lacking companions, the inferred projected distances should therefore be regarded as lower limits, as genuine physical companions may exist at larger separations. Establishing physical association at these distances generally requires wider-area searches and, ideally, spectroscopic confirmation.

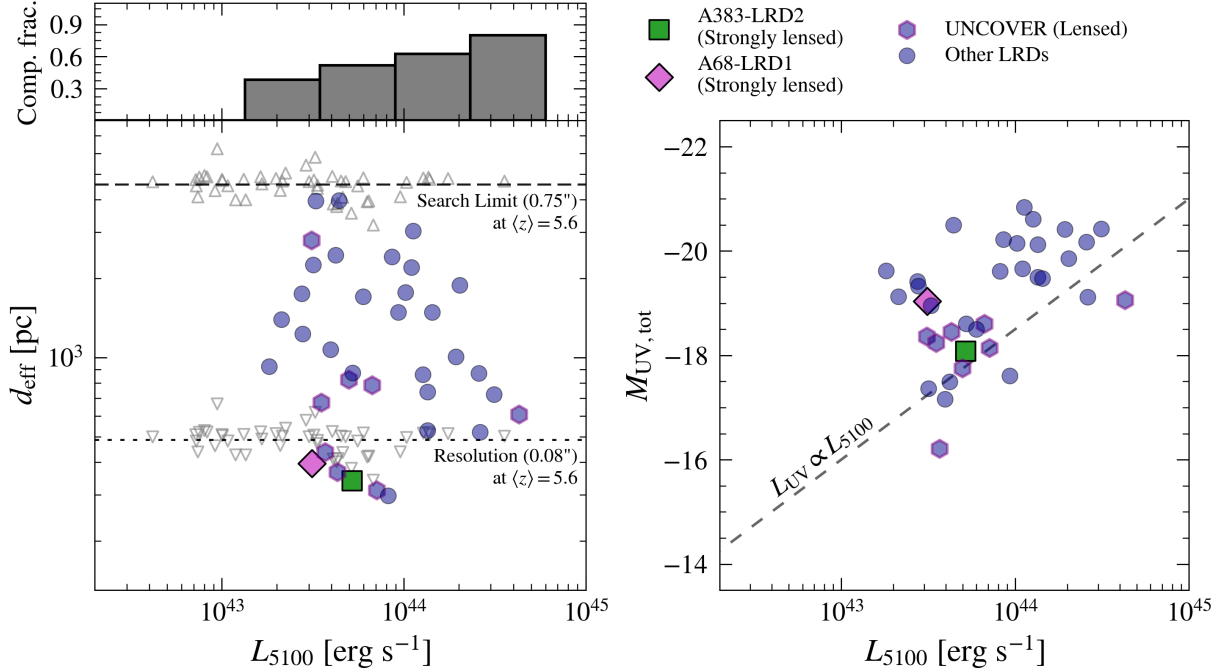


Figure 5. *Left panel:* Effective projected separation between the compact red component and its associated companion(s) as a function of the inferred luminosity L_{5100} . The luminosity is measured using the NIRCam filter closest to rest-frame 5100 Å and converted to a luminosity using the source redshift. The top panel shows the companion fraction as a function of luminosity; we find a striking trend where the companion fraction increases with L_{5100} , reaching nearly 100% completeness for the most luminous LRDs in our sample. *Right panel:* the companion(s) UV magnitude (rest-frame 1500 Å) as a function of L_{5100} , indicating that companions associated with these high-luminosity LRDs are themselves significantly brighter in the UV.

Second, some candidate companions are not included in the formal sample. We mark these features with question marks in Fig. 2. They fall into two distinct categories. One class consists of companions at very small projected separations that are unresolved in unlensed fields. Strongly lensed systems demonstrate that companions can exist at separations that would be extremely difficult to resolve without lensing (J. F. W. Baggen et al. 2025). As companions are typically much fainter than the LRD, they are difficult to identify if they lie within ~ 2 LW pixels. Adopting 2–2.5 pixels as an effective resolution limit corresponds to a physical scale of ~ 500 pc, as indicated in Fig. 5. Systems classified as isolated may therefore host unresolved blue companions at smaller separations. Indeed, in several cases we observe faint blue residual features near the LRD position after subtraction of the red component (Fig. 2). These features are not detected as independent sources by the pipeline but may represent companions at very small separations. The second class consists of sources that are clearly detected at larger projected separations and exhibit morphologies consistent with high-redshift star-forming galaxies, but for which the photometric redshift solutions do not satisfy our statistical consistency criterion. This typically reflects limited band coverage or low

signal-to-noise rather than contradictory redshift constraints. Although these sources are visually compelling and consistent with being physical companions, we exclude them from the formal sample. Including all such candidate companions marked with question marks in Fig. 2 would increase the inferred companion fraction to 72%.

Third, the data are of mixed depth and very faint companions are likely missed in our analysis, particularly at higher redshifts ($z \gtrsim 7$). As the LW flux scales with d_{eff}^{-2} , even very faint companions can produce sufficient radiation to bring the LRD into the direct-collapse regime if they are sufficiently close. In our sample the UV luminosity of the companions and the fraction of LRDs with a detected companion both scale with the L_{5100} luminosity of the LRD (Fig. 5), strongly suggesting that depth effects plague the faint end of the sample. If we limited the sample to LRDs with $L_{5100} > 10^{44}$ erg s $^{-1}$, nearly 100% of objects would have a UV-bright companion. Consistent with this interpretation, LRDs in lensed fields, such as the UNCOVER sample, show a substantially higher companion fraction than those in unlensed fields, reflecting the improved sensitivity to faint, close companions.

Fourth, the star-forming phase required to generate a high LW flux may be short-lived, implying that some systems may be observed after the companion has faded or been disrupted (D. Schaefer 2002).

Finally, the LRD selection does not require that all systems host accreting black holes. A fraction of the population may instead be dominated by compact stellar components, given that the emission from stellar populations in at least a subset of the sources remains largely degenerate with accretion dominated emission, especially at low metallicities and high ionization parameters (N. J. Cleri et al. 2025). Such stellar-dominated systems can reach high central stellar densities and give rise to broad emission lines without requiring an actively accreting black hole (J. F. W. Baggen et al. 2024; C. A. Guia et al. 2024). We should expect “normal” stellar Balmer breaks, consistent with the presence of evolved stellar populations (A. Weibel et al. 2025; B. Wang et al. 2024). Such sources likely represent the earliest phases of dense stellar cores that will evolve into the central regions of massive galaxies at later times (e.g., I. Labb   et al. 2023; J. F. W. Baggen et al. 2023, 2024; C. A. Guia et al. 2024; D. Herrero-Carri  n et al. 2025). The fraction of LRDs that are stellar-dominated remains uncertain. Although a subset resides in overdense environments (T. S. Tanaka et al. 2024; J.-T. Schindler et al. 2025; A. Torralba et al. 2026; J. Matthee et al. 2025; F. D’Eugenio et al. 2026), the clustering and number density of LRDs indicate that most reside in relatively low mass halos (E. Pizzati et al. 2025).

5.3. *Metallicities and Sizes*

In most theoretical models of direct collapse it is assumed that the gas has near-zero metallicity such that H₂ cooling is the dominant channel. Above a critical metallicity of order $\sim 10^{-5} Z_{\odot}$, metal-line cooling is expected to induce fragmentation (M. C. Begelman & M. J. Rees 1978). The scenario described here thus predicts that LRDs had near-zero metallicities during collapse.

Observationally, this expectation appears to be in tension with the properties of at least part of the LRD population. Many LRDs show prominent metal emission lines (e.g. A. Torralba et al. 2025; F. D’Eugenio et al. 2025a; V. Kokorev et al. 2025; I. Labb   et al. 2024; E. Lambrides et al. 2025), indicating that at least some chemical enrichment has occurred in these systems (although the enriched gas could also come from the UV-bright companion, or other gas in the vicinity). At the same time, other LRDs show evidence for low metallicity (R. Maiolino et al. 2025; R. Tripodi et al. 2025), with some LRD spectra dominated by hydrogen and helium

lines and little to no detectable metal emission (A. de Graaff et al. 2025a; L. J. Furtak et al. 2024).

A related prediction concerns sizes. The immediate products of collapse, such as supermassive stars (in self-gravitating disks), quasi-stars or “black hole stars,” are expected to be AU/sub-pc scale and thus unresolved by JWST, even when strongly lensed. In contrast, we measure a wide range of effective sizes for the red components, with a mean effective radius of ~ 200 pc, consistent with stacked rest-frame optical sizes reported by Y. Zhang et al. (2025).

Combined, both the observed metallicities and the range of measured sizes can be naturally reconciled if some star formation and associated enrichment occurred during or after the initial collapse, or during subsequent interactions with nearby companions (see also P. Natarajan et al. 2017). Such evolution would lead to sizes larger than expected for a single compact object and, given the extreme compactness of these systems, enrichment is expected to proceed rapidly. In this picture, signatures of massive stars may be present in the spectra of the red components (e.g., nitrogen emission; D. A. Berg et al. 2025; I. Morel et al. 2025), particularly in spatially resolved or more metal-rich systems.

6. CONCLUSIONS

In this work, we have identified candidate UV-bright companions to a substantial fraction of LRDs (43% increasing to 72% when including tentative companions), assumed a physical connection between the components, and used their luminosities and projected separations to infer the local Lyman-Werner radiation fields experienced by the compact red sources. The inferred radiation fields are sufficiently intense to plausibly suppress molecular cooling and enable rapid collapse to very high densities, in line with established theoretical models. While this agreement does not constitute a proof of the scenario, it demonstrates that the picture is internally consistent and observationally viable.

It is particularly striking that the two most strongly lensed systems in our sample exhibit remarkably similar configurations, each consisting of an extremely compact blue component located only ~ 300 pc from a compact red source. This recurring geometry suggests that the association may not be coincidental. In the framework explored here, the UV-bright component exists first and regulates the formation of the compact red object, though alternative scenarios in which the red component forms first and subsequently triggers nearby star formation remain plausible. The present data do not uniquely determine the direction of causality, but they motivate a unified picture that naturally connects

the observed morphologies, SEDs, and inferred radiation fields.

This concordance picture leads to a set of concrete, testable predictions and motivates theoretical and observational follow-up studies. An important question is whether the observed abundance of LRDs is consistent with theoretical expectations for objects formed through LW-regulated collapse. Early work used cosmological N-body simulations to obtain the number density of close synchronized pairs, and found up to a few $\times 10^{-4}$ cMpc $^{-3}$ at redshift $z \sim 10$ (E. Visbal et al. 2014). Recent observational estimates suggest LRD number densities of $\sim 10^{-4.5}$ cMpc $^{-3}$ $z > 4$ (Y. Ma et al. 2025). Adopting this value, and taking 40 %, as a conservative lower limit on the fraction of LRDs with close UV-bright companions, implies a number density of $\sim 10^{-4.9}$ cMpc $^{-3}$, substantially below the predicted theoretical values. Yet, these theoretical predictions apply to higher redshift, and the expected abundance may decline toward lower redshift as suitable pristine environments become rarer; recent work based on cosmological hydrodynamical simulations and analytic prescriptions also found somewhat lower maximum number densities (H. O’Brennan et al. 2025). Additionally, LRDs in general become increasingly difficult to detect at high redshift. Whether current models quantitatively reproduce the observed number densities of LRDs therefore remains an open question. In addition, simulations of the collapse process and subsequent star formation and enrichment will be highly valuable.

On the observational side, we can expect progress from spatially resolved spectroscopy, ideally for strongly lensed systems such as A383-LRD and A68-LRD. Such observations could measure metallicity and ionization gradients, constrain the degree of radiative shielding between components, and provide accurate sizes (or size limits) of the red components. These data will determine whether the close proximity of UV-bright companions to compact red sources reflects a causal link in their formation or requires an alternative physical origin.

ACKNOWLEDGMENTS

We thank Earl Bellinger, Fabio Pacucci, Andrea Ferrara and Dale Kocevski for useful discussions. This work used the following python packages: `Matplotlib` (J. D. Hunter 2007), `SciPy` (P. Virtanen et al. 2020), `NumPy` (S. van der Walt et al. 2011), `AstroPy` (Astropy Collaboration et al. 2022) and `colossus` (B. Diemer 2018) and `photutils` (L. Bradley et al. 2025).

APPENDIX

APPENDIX A: SOURCES WITH NO IDENTIFIED COMPANION

ID	RA	DEC	z	ID	RA	DEC	z
CEERS-3153	214.9258	52.9457	5.09	JADES-39353	189.2940	62.1531	4.85
CEERS-5760	214.9724	52.9622	5.08	JADES-4685	189.0963	62.2391	7.42
CEERS-6126	214.9234	52.9256	5.29	JADES-12402	53.1327	-27.7655	3.19
CEERS-7000	214.8400	52.8606	3.86	JADES-38562	53.1359	-27.8716	4.82
CEERS-12833	214.9295	52.8879	7.16	JADES-4461	53.2040	-27.7721	7.25
CEERS-13135	214.8868	52.8554	4.95	JADES-12068	53.1265	-27.8181	5.92
CEERS-13748	214.8405	52.8179	6.11	JADES-21598	53.0877	-27.8712	4.74
CEERS-14949	214.9910	52.9165	5.68	JADES-64894	53.0605	-27.8484	5.50
CEERS-18850	214.9278	52.8500	7.48	GOODS-N-4014	189.3001	62.2120	5.23
CEERS-20496	215.0783	52.9485	6.79	GOODS-N-12839	189.3443	62.2634	5.24
CEERS-20777	215.1371	52.9886	5.29	GOODS-N-13733	189.0571	62.2689	5.24
CEERS-23931	214.8171	52.7483	9.94	GOODS-N-14409	189.0721	62.2734	5.14
CEERS-69459	214.8897	52.8330	5.67	GOODS-N-15498	189.2855	62.2808	5.09
CEERS-80072	214.9372	52.9654	5.30	GOODS-N-16813	189.1793	62.2925	5.36
CEERS-81443	214.8307	52.8878	7.76	J1148-18404	177.0580	52.8628	5.01
CEERS-82815	214.8091	52.8685	5.62	J1120-7546	169.9994	6.6547	4.97
CEERS-99879	214.8719	52.8804	5.68	J1120-14389	170.0037	6.7196	4.90
CEERS-111399	214.8968	52.8758	6.13				
CEERS-114801	214.9755	52.9253	5.11				
CEERS-19300	215.0221	52.9208	4.53				
CEERS-23961	214.8997	52.8128	5.00				
CEERS-2015	214.9180	52.9372	4.89				
CEERS-47962	214.8925	52.8569	6.73				
UNCOVER-2008	3.5924	-30.4328	6.74				
UNCOVER-13123 [†]	3.5798	-30.4016	7.04				
UNCOVER-15383 [†]	3.5835	-30.3967	7.04				
UNCOVER-16594 [†]	3.5972	-30.3943	7.04				
UNCOVER-20466	3.6404	-30.3864	8.50				
UNCOVER-28876	3.5696	-30.3732	7.04				
UNCOVER-20698	3.5567	-30.4082	2.42				
UNCOVER-27114	3.5458	-30.3957	5.20				
UNCOVER-49702	3.5477	-30.3337	4.87				

Table 2. [†] A2744 triply lensed LRD: Although a potential companion is identified by the pipeline, we remain cautious. For a genuinely associated companion, all three lensed images are expected to show consistent counterparts. Proper delensing to the source plane using accurate lens models, together with spectroscopic confirmation, is required to assess this. We therefore do not count this object as a reliable companion in our analysis.

A. A STRONGLY LENSED LITTLE RED DOT BEHIND ABEll 68

As part of our search for strongly lensed systems, we identified a new strongly LRD, triply imaged behind the galaxy cluster Abell 68, observed as part of the VENUS collaboration (Program ID: GO 6882; PI: S. Fujimoto). It is visually identified and corresponds to the triply imaged source reported by [J. Richard et al. \(2007\)](#), who measured a spectroscopic redshift of $z = 5.421$ from the Ly α emission line. We do not construct new lens models for this system,

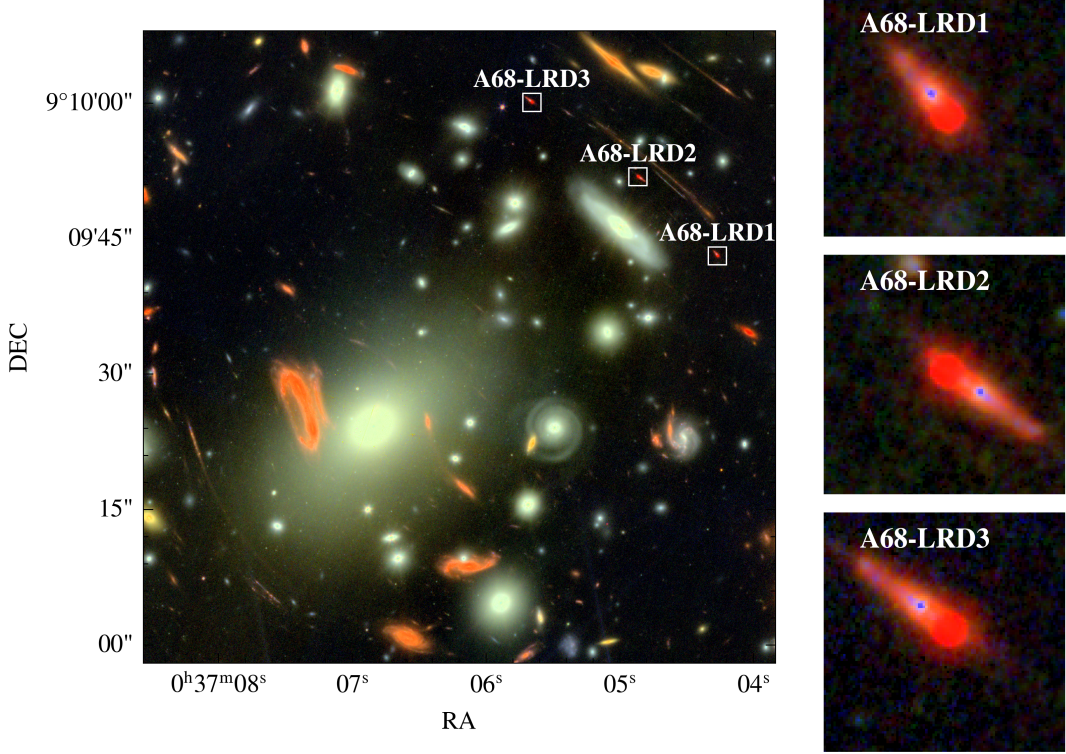


Figure 6. RGB composite of the Abell 68 cluster field, constructed from F444W+F356W (red), F277W+F200W (green), and F150W+F115W+F090W (blue), showing the three lensed images of A68-LRD. The imaging is publicly available from the VENUS collaboration (Program ID: GO 6882; PI: S. Fujimoto).

but instead adopt the magnification estimates from [J. Richard et al. \(2007\)](#), namely $\mu_1 = 12.5 \pm 0.9$, $\mu_2 = 14.3 \pm 0.9$, and $\mu_3 = 11.9 \pm 1.1$. Fig 6 shows the RGB composite image of the galaxy cluster and the three lensed images of A68-LRD. The morphology is remarkably similar to the LRD found behind Abell 383 ([J. F. W. Baggen et al. 2025](#); [M. Golubchik et al. 2025](#)), motivating the concordance picture developed in this work. In this analysis, we perform the measurements on image A68-LRD1.

REFERENCES

Agarwal, B., Dalla Vecchia, C., Johnson, J. L., Khochfar, S., & Paardekooper, J.-P. 2014, MNRAS, 443, 648, doi: [10.1093/mnras/stu1112](https://doi.org/10.1093/mnras/stu1112)

Agarwal, B., Khochfar, S., Johnson, J. L., et al. 2012, MNRAS, 425, 2854, doi: [10.1111/j.1365-2966.2012.21651.x](https://doi.org/10.1111/j.1365-2966.2012.21651.x)

Agarwal, B., Smith, B., Glover, S., Natarajan, P., & Khochfar, S. 2016, MNRAS, 459, 4209, doi: [10.1093/mnras/stw929](https://doi.org/10.1093/mnras/stw929)

Ananna, T. T., Bogdán, Á., Kovács, O. E., Natarajan, P., & Hickox, R. C. 2024, ApJL, 969, L18, doi: [10.3847/2041-8213/ad5669](https://doi.org/10.3847/2041-8213/ad5669)

Astropy Collaboration, Price-Whelan, A. M., Lim, P. L., et al. 2022, ApJ, 935, 167, doi: [10.3847/1538-4357/ac7c74](https://doi.org/10.3847/1538-4357/ac7c74)

Baggen, J. F. W., van Dokkum, P., Labbé, I., & Brammer, G. 2025, arXiv e-prints, arXiv:2512.03239, doi: [10.48550/arXiv.2512.03239](https://doi.org/10.48550/arXiv.2512.03239)

Baggen, J. F. W., van Dokkum, P., Labbé, I., et al. 2023, ApJL, 955, L12, doi: [10.3847/2041-8213/acf5ef](https://doi.org/10.3847/2041-8213/acf5ef)

Baggen, J. F. W., van Dokkum, P., Brammer, G., et al. 2024, ApJL, 977, L13, doi: [10.3847/2041-8213/ad90b8](https://doi.org/10.3847/2041-8213/ad90b8)

Barro, G., Pérez-González, P. G., Kocevski, D., et al. 2025, arXiv e-prints, arXiv:2512.15853, doi: [10.48550/arXiv.2512.15853](https://doi.org/10.48550/arXiv.2512.15853)

Barro, G., Pérez-González, P. G., Kocevski, D. D., et al. 2026, ApJ, 997, 48, doi: [10.3847/1538-4357/ae0704](https://doi.org/10.3847/1538-4357/ae0704)

Begelman, M. C., & Dexter, J. 2025, arXiv e-prints, arXiv:2507.09085, doi: [10.48550/arXiv.2507.09085](https://doi.org/10.48550/arXiv.2507.09085)

Begelman, M. C., & Rees, M. J. 1978, MNRAS, 185, 847, doi: [10.1093/mnras/185.4.847](https://doi.org/10.1093/mnras/185.4.847)

Begelman, M. C., Volonteri, M., & Rees, M. J. 2006, MNRAS, 370, 289, doi: [10.1111/j.1365-2966.2006.10467.x](https://doi.org/10.1111/j.1365-2966.2006.10467.x)

Berg, D. A., Naidu, R. P., Chisholm, J., et al. 2025, arXiv e-prints, arXiv:2511.13591, doi: [10.48550/arXiv.2511.13591](https://doi.org/10.48550/arXiv.2511.13591)

Bezanson, R., Labbe, I., Whitaker, K. E., et al. 2024, ApJ, 974, 92, doi: [10.3847/1538-4357/ad66cf](https://doi.org/10.3847/1538-4357/ad66cf)

Boekholt, T. C. N., Schleicher, D. R. G., Fellhauer, M., et al. 2018, MNRAS, 476, 366, doi: [10.1093/mnras/sty208](https://doi.org/10.1093/mnras/sty208)

Bradley, L., Sipőcz, B., Robitaille, T., et al. 2025, astropy/photutils: 2.2.0, 2.2.0 Zenodo, doi: [10.5281/zenodo.14889440](https://doi.org/10.5281/zenodo.14889440)

Brammer, G. 2023a, msaexp: NIRSpec analysis tools, 0.6.17 Zenodo, doi: [10.5281/zenodo.7299500](https://doi.org/10.5281/zenodo.7299500)

Brammer, G. 2023b, grizli, 1.5.2 Zenodo, doi: [10.5281/ZENODO.1146904](https://doi.org/10.5281/ZENODO.1146904)

Brammer, G. B., van Dokkum, P. G., & Coppi, P. 2008, ApJ, 686, 1503, doi: [10.1086/591786](https://doi.org/10.1086/591786)

Bromm, V., & Loeb, A. 2003, ApJ, 596, 34, doi: [10.1086/377529](https://doi.org/10.1086/377529)

Cenci, E., & Habouzit, M. 2025, MNRAS, 542, 2597, doi: [10.1093/mnras/staf1362](https://doi.org/10.1093/mnras/staf1362)

Chen, C.-H., Ho, L. C., Li, R., & Inayoshi, K. 2025, ApJL, 989, L12, doi: [10.3847/2041-8213/adee0a](https://doi.org/10.3847/2041-8213/adee0a)

Chon, S., Hirano, S., Hosokawa, T., & Yoshida, N. 2016, ApJ, 832, 134, doi: [10.3847/0004-637X/832/2/134](https://doi.org/10.3847/0004-637X/832/2/134)

Chon, S., & Omukai, K. 2020, MNRAS, 494, 2851, doi: [10.1093/mnras/staa863](https://doi.org/10.1093/mnras/staa863)

Chon, S., & Omukai, K. 2025, MNRAS, 539, 2561, doi: [10.1093/mnras/staf598](https://doi.org/10.1093/mnras/staf598)

Cleri, N. J., Olivier, G. M., Backhaus, B. E., et al. 2025, ApJ, 994, 146, doi: [10.3847/1538-4357/ae0f17](https://doi.org/10.3847/1538-4357/ae0f17)

de Graaff, A., Brammer, G., Weibel, A., et al. 2024, arXiv e-prints, arXiv:2409.05948, doi: [10.48550/arXiv.2409.05948](https://doi.org/10.48550/arXiv.2409.05948)

de Graaff, A., Rix, H.-W., Naidu, R. P., et al. 2025a, arXiv e-prints, arXiv:2503.16600, doi: [10.48550/arXiv.2503.16600](https://doi.org/10.48550/arXiv.2503.16600)

de Graaff, A., Hviding, R. E., Naidu, R. P., et al. 2025b, arXiv e-prints, arXiv:2511.21820, doi: [10.48550/arXiv.2511.21820](https://doi.org/10.48550/arXiv.2511.21820)

D'Eugenio, F., Nelson, E., Ji, X., et al. 2025a, arXiv e-prints, arXiv:2510.00101, doi: [10.48550/arXiv.2510.00101](https://doi.org/10.48550/arXiv.2510.00101)

D'Eugenio, F., Maiolino, R., Perna, M., et al. 2025b, arXiv e-prints, arXiv:2503.11752, doi: [10.48550/arXiv.2503.11752](https://doi.org/10.48550/arXiv.2503.11752)

D'Eugenio, F., Juodžbalis, I., Ji, X., et al. 2026, MNRAS, 545, staf2117, doi: [10.1093/mnras/staf2117](https://doi.org/10.1093/mnras/staf2117)

Devecchi, B., & Volonteri, M. 2009, ApJ, 694, 302, doi: [10.1088/0004-637X/694/1/302](https://doi.org/10.1088/0004-637X/694/1/302)

Diemer, B. 2018, ApJS, 239, 35, doi: [10.3847/1538-4365/aaee8c](https://doi.org/10.3847/1538-4365/aaee8c)

Dijkstra, M., Ferrara, A., & Mesinger, A. 2014, MNRAS, 442, 2036, doi: [10.1093/mnras/stu1007](https://doi.org/10.1093/mnras/stu1007)

Dijkstra, M., Haiman, Z., Mesinger, A., & Wyithe, J. S. B. 2008, MNRAS, 391, 1961, doi: [10.1111/j.1365-2966.2008.14031.x](https://doi.org/10.1111/j.1365-2966.2008.14031.x)

Draine, B. T., & Bertoldi, F. 1996, ApJ, 468, 269, doi: [10.1086/177689](https://doi.org/10.1086/177689)

Eisenstein, D. J., Willott, C., Alberts, S., et al. 2023, arXiv e-prints, arXiv:2306.02465, doi: [10.48550/arXiv.2306.02465](https://doi.org/10.48550/arXiv.2306.02465)

Fei, Q., Fujimoto, S., Naidu, R. P., et al. 2025, arXiv e-prints, arXiv:2509.20452, doi: [10.48550/arXiv.2509.20452](https://doi.org/10.48550/arXiv.2509.20452)

Ferrara, A., Salvadori, S., Yue, B., & Schleicher, D. 2014, MNRAS, 443, 2410, doi: [10.1093/mnras/stu1280](https://doi.org/10.1093/mnras/stu1280)

Finkelstein, S. L., Bagley, M. B., Ferguson, H. C., et al. 2023, ApJL, 946, L13, doi: [10.3847/2041-8213/acade4](https://doi.org/10.3847/2041-8213/acade4)

Furtak, L. J., Labb  , I., Zitrin, A., et al. 2024, Nature, 628, 57, doi: [10.1038/s41586-024-07184-8](https://doi.org/10.1038/s41586-024-07184-8)

Golubchik, M., Furtak, L. J., Allingham, J. F. V., et al. 2025, arXiv e-prints, arXiv:2512.02117, doi: [10.48550/arXiv.2512.02117](https://doi.org/10.48550/arXiv.2512.02117)

Greene, J. E., Labbe, I., Goulding, A. D., et al. 2024, ApJ, 964, 39, doi: [10.3847/1538-4357/ad1e5f](https://doi.org/10.3847/1538-4357/ad1e5f)

Greif, T. H., Springel, V., White, S. D. M., et al. 2011, ApJ, 737, 75, doi: [10.1088/0004-637X/737/2/75](https://doi.org/10.1088/0004-637X/737/2/75)

Guia, C. A., Pacucci, F., & Kocevski, D. D. 2024, Research Notes of the American Astronomical Society, 8, 207, doi: [10.3847/2515-5172/ad7262](https://doi.org/10.3847/2515-5172/ad7262)

Haemmerl  , L., Woods, T. E., Klessen, R. S., Heger, A., & Whalen, D. J. 2018, MNRAS, 474, 2757, doi: [10.1093/mnras/stx2919](https://doi.org/10.1093/mnras/stx2919)

Haiman, Z. 2013, in Astrophysics and Space Science Library, Vol. 396, The First Galaxies, ed. T. Wiklind, B. Mobasher, & V. Bromm, 293, doi: [10.1007/978-3-642-32362-1_6](https://doi.org/10.1007/978-3-642-32362-1_6)

Haiman, Z., Rees, M. J., & Loeb, A. 1997, ApJ, 476, 458, doi: [10.1086/303647](https://doi.org/10.1086/303647)

Heintz, K. E., Brammer, G. B., Watson, D., et al. 2024, arXiv e-prints, arXiv:2404.02211, doi: [10.48550/arXiv.2404.02211](https://doi.org/10.48550/arXiv.2404.02211)

Herrero-Carri  n, D., Spinoso, D., Izquierdo-Villalba, D., et al. 2025, arXiv e-prints, arXiv:2511.10725, doi: [10.48550/arXiv.2511.10725](https://doi.org/10.48550/arXiv.2511.10725)

Hirano, S., Hosokawa, T., Yoshida, N., & Kuiper, R. 2017, Science, 357, 1375, doi: [10.1126/science.aai9119](https://doi.org/10.1126/science.aai9119)

Hosokawa, T., Hirano, S., Kuiper, R., et al. 2016, ApJ, 824, 119, doi: [10.3847/0004-637X/824/2/119](https://doi.org/10.3847/0004-637X/824/2/119)

Hunter, J. D. 2007, Computing in Science and Engineering, 9, 90, doi: [10.1109/MCSE.2007.55](https://doi.org/10.1109/MCSE.2007.55)

Hviding, R. E., de Graaff, A., Miller, T. B., et al. 2025, arXiv e-prints, arXiv:2506.05459, doi: [10.48550/arXiv.2506.05459](https://doi.org/10.48550/arXiv.2506.05459)

Inayoshi, K., & Haiman, Z. 2014, MNRAS, 445, 1549, doi: [10.1093/mnras/stu1870](https://doi.org/10.1093/mnras/stu1870)

Inayoshi, K., & Ho, L. C. 2025, arXiv e-prints, arXiv:2512.03130, doi: [10.48550/arXiv.2512.03130](https://doi.org/10.48550/arXiv.2512.03130)

Inayoshi, K., & Maiolino, R. 2025, ApJL, 980, L27, doi: [10.3847/2041-8213/adaebd](https://doi.org/10.3847/2041-8213/adaebd)

Inayoshi, K., Visbal, E., & Haiman, Z. 2020, ARA&A, 58, 27, doi: [10.1146/annurev-astro-120419-014455](https://doi.org/10.1146/annurev-astro-120419-014455)

Jeon, J., Liu, B., Bromm, V., et al. 2025, arXiv e-prints, arXiv:2508.14155, doi: [10.48550/arXiv.2508.14155](https://doi.org/10.48550/arXiv.2508.14155)

Ji, X., Maiolino, R.,   bler, H., et al. 2025, MNRAS, doi: [10.1093/mnras/staf1867](https://doi.org/10.1093/mnras/staf1867)

Juod  balis, I., Maiolino, R., Baker, W. M., et al. 2024, arXiv e-prints, arXiv:2403.03872, doi: [10.48550/arXiv.2403.03872](https://doi.org/10.48550/arXiv.2403.03872)

Kashino, D., Lilly, S. J., Matthee, J., et al. 2023, ApJ, 950, 66, doi: [10.3847/1538-4357/acc588](https://doi.org/10.3847/1538-4357/acc588)

Kido, D., Ioka, K., Hotokezaka, K., Inayoshi, K., & Irwin, C. M. 2025, MNRAS, 544, 3407, doi: [10.1093/mnras/staf1898](https://doi.org/10.1093/mnras/staf1898)

Knudsen, K. K., Richard, J., Jauzac, M., et al. 2025, arXiv e-prints, arXiv:2512.05097, doi: [10.48550/arXiv.2512.05097](https://doi.org/10.48550/arXiv.2512.05097)

Kocevski, D. D., Finkelstein, S. L., Barro, G., et al. 2024, arXiv e-prints, arXiv:2404.03576, doi: [10.48550/arXiv.2404.03576](https://doi.org/10.48550/arXiv.2404.03576)

Kokorev, V., Chisholm, J., Naidu, R. P., et al. 2025, arXiv e-prints, arXiv:2511.07515, doi: [10.48550/arXiv.2511.07515](https://doi.org/10.48550/arXiv.2511.07515)

Labb  , I., van Dokkum, P., Nelson, E., et al. 2023, Nature, 616, 266, doi: [10.1038/s41586-023-05786-2](https://doi.org/10.1038/s41586-023-05786-2)

Labbe, I., Greene, J. E., Matthee, J., et al. 2024, arXiv e-prints, arXiv:2412.04557, doi: [10.48550/arXiv.2412.04557](https://doi.org/10.48550/arXiv.2412.04557)

Lambrides, E., Larson, R., Hutchison, T., et al. 2025, arXiv e-prints, arXiv:2509.09607, doi: [10.48550/arXiv.2509.09607](https://doi.org/10.48550/arXiv.2509.09607)

Latif, M. A., Bovino, S., Van Borm, C., et al. 2014, MNRAS, 443, 1979, doi: [10.1093/mnras/stu1230](https://doi.org/10.1093/mnras/stu1230)

Latif, M. A., Niemeyer, J. C., & Schleicher, D. R. G. 2014, MNRAS, 440, 2969, doi: [10.1093/mnras/stu489](https://doi.org/10.1093/mnras/stu489)

Latif, M. A., Omukai, K., Habouzit, M., Schleicher, D. R. G., & Volonteri, M. 2016, ApJ, 823, 40, doi: [10.3847/0004-637X/823/1/40](https://doi.org/10.3847/0004-637X/823/1/40)

Latif, M. A., Schleicher, D. R. G., Schmidt, W., & Niemeyer, J. 2013, MNRAS, 433, 1607, doi: [10.1093/mnras/stt834](https://doi.org/10.1093/mnras/stt834)

Leung, G. C. K., Finkelstein, S. L., P  rez-Gonz  lez, P. G., et al. 2025, ApJ, 992, 26, doi: [10.3847/1538-4357/adcce](https://doi.org/10.3847/1538-4357/adcce)

Liu, H., Jiang, Y.-F., Quataert, E., Greene, J. E., & Ma, Y. 2025, ApJ, 994, 113, doi: [10.3847/1538-4357/ae0c19](https://doi.org/10.3847/1538-4357/ae0c19)

Ma, Y., Greene, J. E., Setton, D. J., et al. 2025, arXiv e-prints, arXiv:2504.08032, doi: [10.48550/arXiv.2504.08032](https://doi.org/10.48550/arXiv.2504.08032)

Machacek, M. E., Bryan, G. L., & Abel, T. 2001, ApJ, 548, 509, doi: [10.1086/319014](https://doi.org/10.1086/319014)

Maiolino, R., Uebler, H., D'Eugenio, F., et al. 2025, arXiv e-prints, arXiv:2505.22567, doi: [10.48550/arXiv.2505.22567](https://doi.org/10.48550/arXiv.2505.22567)

Matthee, J. 2025, *Contemporary Physics*, 66, 116, doi: [10.1080/00107514.2025.2586370](https://doi.org/10.1080/00107514.2025.2586370)

Matthee, J., Naidu, R. P., Brammer, G., et al. 2024, *ApJ*, 963, 129, doi: [10.3847/1538-4357/ad2345](https://doi.org/10.3847/1538-4357/ad2345)

Matthee, J., Naidu, R. P., Kotiwale, G., et al. 2025, *ApJ*, 988, 246, doi: [10.3847/1538-4357/ade886](https://doi.org/10.3847/1538-4357/ade886)

Mérida, R. M., Gaspar, G., Sawicki, M., et al. 2025, *A&A*, 698, A317, doi: [10.1051/0004-6361/202553943](https://doi.org/10.1051/0004-6361/202553943)

Morel, I., Schaefer, D., Marques-Chaves, R., et al. 2025, arXiv e-prints, arXiv:2511.20484, doi: [10.48550/arXiv.2511.20484](https://doi.org/10.48550/arXiv.2511.20484)

Naidu, R. P., Matthee, J., Katz, H., et al. 2025, arXiv e-prints, arXiv:2503.16596, doi: [10.48550/arXiv.2503.16596](https://doi.org/10.48550/arXiv.2503.16596)

Natarajan, P. 2011, *Bulletin of the Astronomical Society of India*, 39, 145, doi: [10.48550/arXiv.1104.4797](https://doi.org/10.48550/arXiv.1104.4797)

Natarajan, P., Pacucci, F., Ferrara, A., et al. 2017, *ApJ*, 838, 117, doi: [10.3847/1538-4357/aa6330](https://doi.org/10.3847/1538-4357/aa6330)

O'Brennan, H., Regan, J. A., Brennan, J., et al. 2025, *The Open Journal of Astrophysics*, 8, 88, doi: [10.33232/001c.141953](https://doi.org/10.33232/001c.141953)

Oesch, P. A., Brammer, G., Naidu, R. P., et al. 2023, *MNRAS*, 525, 2864, doi: [10.1093/mnras/stad2411](https://doi.org/10.1093/mnras/stad2411)

Oh, S. P., & Haiman, Z. 2002, *ApJ*, 569, 558, doi: [10.1086/339393](https://doi.org/10.1086/339393)

Omukai, K. 2001, *ApJ*, 546, 635, doi: [10.1086/318296](https://doi.org/10.1086/318296)

Omukai, K., Schneider, R., & Haiman, Z. 2008, *ApJ*, 686, 801, doi: [10.1086/591636](https://doi.org/10.1086/591636)

Pacucci, F., Ferrara, A., & Kocevski, D. D. 2026, arXiv e-prints, arXiv:2601.14368, doi: [10.48550/arXiv.2601.14368](https://doi.org/10.48550/arXiv.2601.14368)

Peebles, P. J. E. 1993, *Principles of Physical Cosmology*, doi: [10.1515/9780691206721](https://doi.org/10.1515/9780691206721)

Peng, C. Y., Ho, L. C., Impey, C. D., & Rix, H.-W. 2002, *AJ*, 124, 266, doi: [10.1086/340952](https://doi.org/10.1086/340952)

Peng, C. Y., Ho, L. C., Impey, C. D., & Rix, H.-W. 2010, *AJ*, 139, 2097, doi: [10.1088/0004-6256/139/6/2097](https://doi.org/10.1088/0004-6256/139/6/2097)

Pérez-González, P. G., Barro, G., Rieke, G. H., et al. 2024, *ApJ*, 968, 4, doi: [10.3847/1538-4357/ad38bb](https://doi.org/10.3847/1538-4357/ad38bb)

Pizzati, E., Hennawi, J. F., Schaye, J., et al. 2025, *MNRAS*, 539, 2910, doi: [10.1093/mnras/staf660](https://doi.org/10.1093/mnras/staf660)

Planck Collaboration VI. 2020, *A&A*, 641, A6, doi: [10.1051/0004-6361/201833910](https://doi.org/10.1051/0004-6361/201833910)

Regan, J. A., & Haehnelt, M. G. 2009, *MNRAS*, 396, 343, doi: [10.1111/j.1365-2966.2009.14579.x](https://doi.org/10.1111/j.1365-2966.2009.14579.x)

Regan, J. A., Visbal, E., Wise, J. H., et al. 2017, *Nature Astronomy*, 1, 0075, doi: [10.1038/s41550-017-0075](https://doi.org/10.1038/s41550-017-0075)

Richard, J., Kneib, J.-P., Jullo, E., et al. 2007, *ApJ*, 662, 781, doi: [10.1086/517875](https://doi.org/10.1086/517875)

Rieke, M. J., Robertson, B., Tacchella, S., et al. 2023, *ApJS*, 269, 16, doi: [10.3847/1538-4365/acf44d](https://doi.org/10.3847/1538-4365/acf44d)

Rinaldi, P., Bonaventura, N., Rieke, G. H., et al. 2024, arXiv e-prints, arXiv:2411.14383, doi: [10.48550/arXiv.2411.14383](https://doi.org/10.48550/arXiv.2411.14383)

Rusakov, V., Watson, D., Nikopoulos, G. P., et al. 2025, arXiv e-prints, arXiv:2503.16595, doi: [10.48550/arXiv.2503.16595](https://doi.org/10.48550/arXiv.2503.16595)

Santarelli, A. D., Campbell, C. B., Farag, E., et al. 2025a, arXiv e-prints, arXiv:2510.11772, doi: [10.48550/arXiv.2510.11772](https://doi.org/10.48550/arXiv.2510.11772)

Santarelli, A. D., Farag, E., Bellinger, E. P., et al. 2025b, arXiv e-prints, arXiv:2510.17952, doi: [10.48550/arXiv.2510.17952](https://doi.org/10.48550/arXiv.2510.17952)

Schaerer, D. 2002, *A&A*, 382, 28, doi: [10.1051/0004-6361:20011619](https://doi.org/10.1051/0004-6361:20011619)

Schindler, J.-T., Hennawi, J. F., Davies, F. B., et al. 2025, *Nature Astronomy*, 9, 1732, doi: [10.1038/s41550-025-02660-1](https://doi.org/10.1038/s41550-025-02660-1)

Scoggins, M. T., & Haiman, Z. 2024, *MNRAS*, 531, 4584, doi: [10.1093/mnras/stae1449](https://doi.org/10.1093/mnras/stae1449)

Setton, D. J., Greene, J. E., de Graaff, A., et al. 2024, arXiv e-prints, arXiv:2411.03424, doi: [10.48550/arXiv.2411.03424](https://doi.org/10.48550/arXiv.2411.03424)

Shang, C., Bryan, G. L., & Haiman, Z. 2010, *MNRAS*, 402, 1249, doi: [10.1111/j.1365-2966.2009.15960.x](https://doi.org/10.1111/j.1365-2966.2009.15960.x)

Sneppen, A., Watson, D., Matthews, J. H., et al. 2026, arXiv e-prints, arXiv:2601.18864, <https://arxiv.org/abs/2601.18864>

Suess, K. A., Weaver, J. R., Price, S. H., et al. 2024, *ApJ*, 976, 101, doi: [10.3847/1538-4357/ad75fe](https://doi.org/10.3847/1538-4357/ad75fe)

Sugimura, K., Omukai, K., & Inoue, A. K. 2014, *MNRAS*, 445, 544, doi: [10.1093/mnras/stu1778](https://doi.org/10.1093/mnras/stu1778)

Sullivan, J., Haiman, Z., Kulkarni, M., & Visbal, E. 2025, *MNRAS*, 542, 822, doi: [10.1093/mnras/staf1269](https://doi.org/10.1093/mnras/staf1269)

Sun, W. Q., Naidu, R. P., Matthee, J., et al. 2026, arXiv e-prints, arXiv:2601.20929, <https://arxiv.org/abs/2601.20929>

Tanaka, T. S., Silverman, J. D., Shimasaku, K., et al. 2024, arXiv e-prints, arXiv:2412.14246, doi: [10.48550/arXiv.2412.14246](https://doi.org/10.48550/arXiv.2412.14246)

Torralba, A., Matthee, J., Pezzulli, G., et al. 2025, arXiv e-prints, arXiv:2510.00103, doi: [10.48550/arXiv.2510.00103](https://doi.org/10.48550/arXiv.2510.00103)

Torralba, A., Matthee, J., Pezzulli, G., et al. 2026, *A&A*, 705, A147, doi: [10.1051/0004-6361/202555596](https://doi.org/10.1051/0004-6361/202555596)

Tripodi, R., Martis, N., Markov, V., et al. 2025, *Nature Communications*, 16, 9830, doi: [10.1038/s41467-025-65070-x](https://doi.org/10.1038/s41467-025-65070-x)

van der Walt, S., Colbert, S. C., & Varoquaux, G. 2011, Computing in Science and Engineering, 13, 22, doi: [10.1109/MCSE.2011.37](https://doi.org/10.1109/MCSE.2011.37)

Virtanen, P., Gommers, R., Oliphant, T. E., et al. 2020, Nature Methods, 17, 261, doi: [10.1038/s41592-019-0686-2](https://doi.org/10.1038/s41592-019-0686-2)

Visbal, E., Haiman, Z., & Bryan, G. L. 2014, MNRAS, 445, 1056, doi: [10.1093/mnras/stu1794](https://doi.org/10.1093/mnras/stu1794)

Volonteri, M. 2010, A&A Rv, 18, 279, doi: [10.1007/s00159-010-0029-x](https://doi.org/10.1007/s00159-010-0029-x)

Volonteri, M., & Begelman, M. C. 2010, MNRAS, 409, 1022, doi: [10.1111/j.1365-2966.2010.17359.x](https://doi.org/10.1111/j.1365-2966.2010.17359.x)

Volonteri, M., & Rees, M. J. 2005, ApJ, 633, 624, doi: [10.1086/466521](https://doi.org/10.1086/466521)

Wang, B., Leja, J., de Graaff, A., et al. 2024, ApJL, 969, L13, doi: [10.3847/2041-8213/ad55f7](https://doi.org/10.3847/2041-8213/ad55f7)

Weaver, J. R., Cutler, S. E., Pan, R., et al. 2024, ApJS, 270, 7, doi: [10.3847/1538-4365/ad07e0](https://doi.org/10.3847/1538-4365/ad07e0)

Weibel, A., de Graaff, A., Setton, D. J., et al. 2025, ApJ, 983, 11, doi: [10.3847/1538-4357/adab7a](https://doi.org/10.3847/1538-4357/adab7a)

Wise, J. H., Regan, J. A., O'Shea, B. W., et al. 2019, Nature, 566, 85, doi: [10.1038/s41586-019-0873-4](https://doi.org/10.1038/s41586-019-0873-4)

Wolcott-Green, J., Haiman, Z., & Bryan, G. L. 2011, MNRAS, 418, 838, doi: [10.1111/j.1365-2966.2011.19538.x](https://doi.org/10.1111/j.1365-2966.2011.19538.x)

Wolcott-Green, J., Haiman, Z., & Bryan, G. L. 2017, MNRAS, 469, 3329, doi: [10.1093/mnras/stx167](https://doi.org/10.1093/mnras/stx167)

Wright, L., Whitaker, K. E., Weaver, J. R., et al. 2024, ApJL, 964, L10, doi: [10.3847/2041-8213/ad2b6d](https://doi.org/10.3847/2041-8213/ad2b6d)

Yanagisawa, H., Ouchi, M., Golubchik, M., et al. 2026, arXiv e-prints, arXiv:2601.06015, doi: [10.48550/arXiv.2601.06015](https://doi.org/10.48550/arXiv.2601.06015)

Yoshida, N., Abel, T., Hernquist, L., & Sugiyama, N. 2003, ApJ, 592, 645, doi: [10.1086/375810](https://doi.org/10.1086/375810)

Zhang, Y., Ding, X., Yang, L., et al. 2025, arXiv e-prints, arXiv:2510.25830, doi: [10.48550/arXiv.2510.25830](https://doi.org/10.48550/arXiv.2510.25830)

Zwick, L., Tiede, C., & Mayer, L. 2025, arXiv e-prints, arXiv:2507.22014, doi: [10.48550/arXiv.2507.22014](https://doi.org/10.48550/arXiv.2507.22014)